December 2020

Effects of Phase Decomposition on the Strength Of CoCrFeMnNi High Entropy Alloy

Fredrick Christopher Monroe
Clemson University, panamerican711@gmail.com

Recommended Citation

Monroe, Fredrick Christopher, "Effects of Phase Decomposition on the Strength Of CoCrFeMnNi High Entropy Alloy" (2020). *All Theses*. 3471.
https://tigerprints.clemson.edu/all_theses/3471

EFFECTS OF PHASE DECOMPOSITION ON THE STRENGTH OF CoCrFeMnNi HIGH ENTROPY ALLOY

A Thesis
Presented to
the Graduate School of
Clemson University

In Partial Fulfillment
of the Requirements for the Degree
Master of Science
Mechanical Engineering

by
Fredrick C. Monroe
December 2020

Accepted by:
Dr. Garrett Pataky, Committee Chair
Dr. Marian Kennedy
Dr. Lonny Thompson
Dr. Huijuan Zhao

Abstract

CoCrFeMnNi high entropy alloy (HEA) serves as a model material that researchers can utilize to gain better understanding of HEA-specific characteristics. When considering CoCrFeMnNi and other HEAs for load-bearing applications, it is necessary to understand possible phase decomposition and its potential influence on mechanical behavior. The aim of this study is to describe phase decomposition in coarse-grained equiatomic CoCrFeMnNi HEA after aging 360 h at 610 °C and 720 h at 700 °C, and show how the reported secondary phases influenced its mechanical behavior via Vickers microhardness and quasi-static tensile experimentation. A Cr-rich phase and MnS inclusion were observed in CoCrFeMnNi aged for 360 h at 610 °C. The magnitude of hardness for this aged material was statistically similar to that of the unaged material, indicating that the Cr-rich phase and MnS precipitates were too small to significantly affect the material hardness. Formation of Cr-rich phase resulted in precipitation strengthening where the yield strength increased by 9% with no significant loss in ductility. Precipitation of Cr-rich, FeCo-rich, and FeCr-rich phases and the MnS inclusion were observed after aging 720 h at 700 °C, resulting in a substantial decrease in yield strength from 291 MPa to 130 MPa. The ultimate tensile strength exhibited a shallower decline due in part to strength preservation via the extensive work hardening ability of CoCrFeMnNi. The significant decrease in strength was accompanied by reduction in ductility due to the overall brittle nature of the secondary phases and severe softening resulting from segregation of Ni. The effects of phase decomposition on the mechanical properties of CoCrFeMnNi after aging 720 h at 700 °C are consistent with reports concerning phase decomposed austenitic stainless steel, namely degradation of the material’s strength and ductility.

Acknowledgements

I am eternally grateful to God my Father. Throughout this endeavor, You have continually blessed me with an abundant measure of peace, joy, good counsel, and protection. Successful completion of my master's studies would not have been possible without Your hand over my life.

I express my sincerest thanks to my advisor, Dr. Garrett J. Pataky. Thank you for encouraging me to keep going, even when I felt that I could not. I am grateful for your support, patience, and guidance throughout my master's studies. Having had the opportunity to share space with you has been a truly rewarding experience.

My thanks to Dr. Marian Kennedy, Dr. Lonny Thompson, and Dr. Huijuan Zhao for agreeing to be a part of my committee and helping further my research.

I would like to thank Sean Lam for his assistance in microhardness experimentation; Dr. Atul Kelkar for allowing me to use the Carbolite-Gero Laboratory Chamber Furnace; Jae Lowe and his students for their assistance in microhardness experimentation; George Wetzel and the Advanced Materials Research Laboratory for assistance in microstructural analysis of the materials used in this study; the staff of the Fluor Daniel Machine Shop; and the staff at Clemson's Machining and Technical Services.

To my colleagues and friends in the FRAME Lab – Mitra Shabani, Kaitlynn Conway, Ben Smith, Jacob Biddlecom, Matt Williams, Muhammed Kose, and Benjamin Elbrecht – thank you all for your support and for making yourselves available whenever I needed help. Each one of you helped make my time at Clemson University even more enjoyable and rewarding.

A special thanks to Dr. Joshua Summers, Trish Nigro, and Katheryn Poole. I cannot thank you enough for your unwavering support and encouragement. You welcomed me with open arms and made Clemson University feel like my home.

Finally, I would like to thank my friends, family, and my partner, Michael. Thank you for your love and support. Thank you for believing in me.

Table of Contents

Table of Contents (Continued)

Page

List of Tables

Table Page

List of Figures

List of Tables (Continued)

Chapter 1. Introduction

1.1. Overview of High Entropy Alloys

Conventional alloy development is largely restricted to a single-principal element approach. Consequently, metallurgical knowledge is skewed towards unary and binary alloy systems with little to no knowledge on more complex compositions [1]. Furthermore, according to Cantor et al. [2] the conventional alloying method limits the scope of discovery for new materials. They estimate the number of possible conventional alloys to be on the order of 10^{11} which pales in comparison to the total number of possible alloys, estimated to be around 10^{78} [2].

Multi-principal element alloys (MPEAs) are a new class of metallic material that, unlike conventional alloys, contain multiple principal elements in equal or near-equal concentration. This novel alloying method allows the expansion of metallurgical knowledge beyond that of traditional alloy systems [1], and vastly increases the opportunities for new alloy discoveries [3–5]. The total number of possible MPEAs can be estimated via the binomial coefficient shown in Equation (1), where *N* is the number of elements and *P* is the number of principal elements.

$$\binom{N}{P} = \frac{N!}{P!(N-P)!} \tag{1}$$

Yeh et al. [3] showed that a random selection of 13 elements with 5 to 13 equiatomic principle elements yields 7,099 alloy systems. Generally, as the number of principal elements increases, the total number of possible equiatomic compositions increases exponentially as shown in Figure 1 [4]. The inset of the figure shows a representative phase diagram. The vertices of the phase diagram denote areas of high concentration of a single element and corresponds to conventional alloys. The interior denotes alloys with equiatomic or near-equiatomic compositions and corresponds to MPEAs.

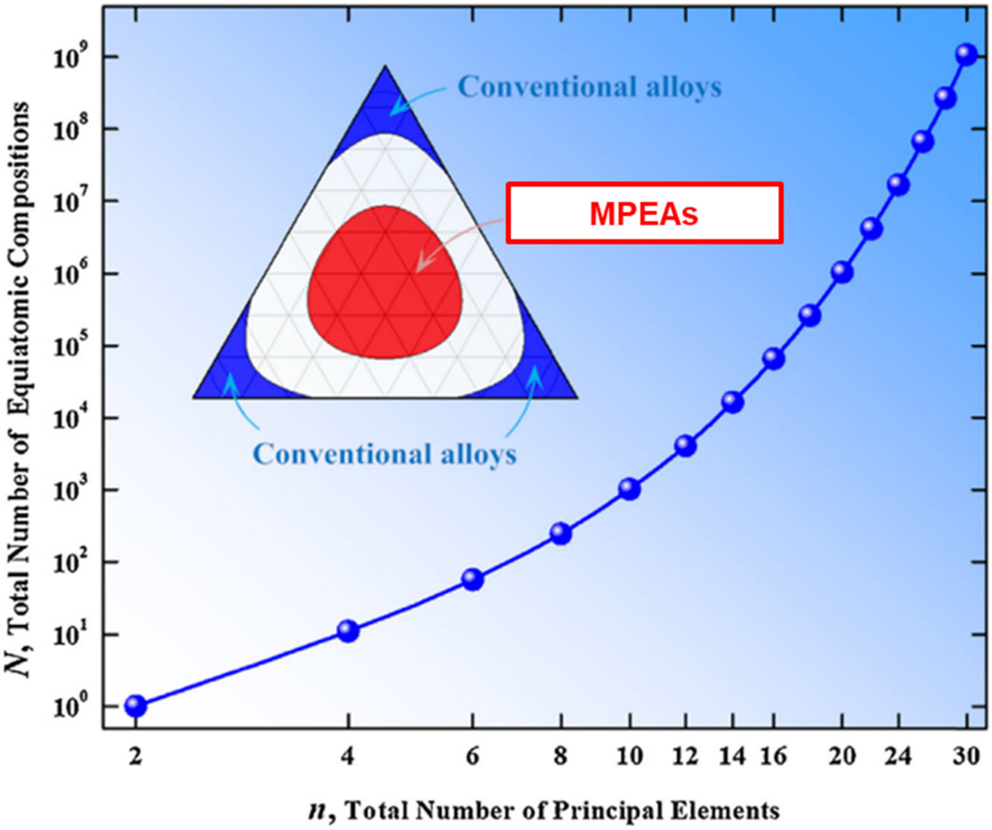

Figure 1: Possible equiatomic compositions as a function of number of principal elements [4].

A phase is any part of a material that has uniform physical and chemical characteristics [6]. A secondary phase or precipitate is any new phase distinguished from the original, parent phase. Conventional understanding of physical metallurgy and phase diagrams suggest the formation of brittle, secondary phases in MPEAs that would render the alloys unsuitable for practical application [3,7–9]. Therefore, early MPEA studies focused on the development of single-phase alloys to avoid secondary phase formation and retain attractive characteristics such as high strength and good ductility found in other conventional alloys [3,10].

Cantor et al. [1] and Yeh et al. [3] independently developed the first single-phase MPEAs in 2004. Yeh et al. [3] hypothesized that single-phase formation in these complex alloys is due to an apparent relationship between high configurational entropy and phase stability. This hypothesis is known in literature as the entropic stabilization or high-entropy effect.

Entropy (S) is a measure of thermal energy in a system that is unavailable to do work. Since work is obtained from molecular motion, entropy can be further defined as a measure of randomness or disorder in the arrangements of atoms and molecules [6,11,12]. Configurational entropy (S_{conf}) is the portion of entropy given as the discrete representative positions of atoms and molecules in a system [12,13]. Equation (2) shows Boltzmann's model describing the relationship between a system's entropy and its complexity [3,12] where Boltzmann's constant, k, has a value of 1.38×10^{-23} J/K and W is the number of possible microscopic states, or atomic arrangements, that can exist in a system. W is equivalent to n^N (where N is the number of particles randomly distributed within a number of elements n).

$$S_{conf} = k \ln W \tag{2}$$

As more atoms and molecules are introduced into a mixture, the number of distinct possible atomic arrangements increases [9,14,15]. It follows then that the configurational entropy of an alloy increases with increasing elements, as shown by Equation (3), where R is the universal gas constant and n is the number of elements.

$$S_{conf} = R \ln n \tag{3}$$

Yeh et al. [3] suggested that most secondary phases possess a magnitude of S_{conf} less than 1.6R. Therefore, by developing an alloy with magnitude of S_{conf} greater than or equal to 1.6R, the microstructure is thermodynamically stabilized against secondary phase formation. Based on this entropic stabilization hypothesis, the first examples of MPEAs are known as high entropy alloys (HEAs). HEAs are a specific subclass of MPEAs defined entropically as possessing configurational entropy greater than or equal to 1.5R [3,16,17]; and defined compositionally as containing at least five elements in concentrations of 5 – 35 at.% [3].

Initially widely accepted [3,7,18–22], it has been proven that high entropy alone does not guarantee the formation of stable, single-phase solid solutions. Some alloys that satisfy one or both HEA definitions fail to form stable solid solutions and/or undergo secondary phase formation (phase decomposition) given certain conditions (e.g. heat treatment, deformation, etc.) [23–32]. Otto et al. [33] concluded in their study that entropy alone is not able to overcome other forces that govern phase stability, such as enthalpy. The failure of high entropy to guarantee the formation of solid solution phases in certain alloys could be related to various thermodynamic and kinetic factors [9] not discussed in this thesis. Miracle et al. [10] found that most of the discovered HEAs do in fact possess multi-phase microstructures. Based on current understanding of secondary phase formation in these alloys, there has been a shift away from the development of single-phase HEAs to that of complex HEAs with desirable multi-phase microstructures [34–36]. Alternative names to "high entropy alloys" have also been introduced including complex concentrated alloys (CCAs) and baseless alloys (BAs) [10,37,38]. Since its introduction, the MPEA field has expanded to include both single-phase and multi-phase alloys, and alloys with as few as three principle equiatomic elements [37].

Research on high entropy alloys has increased substantially [9,39] due to their exceptional material properties including high strength [19,40,41], high hardness [24,42,43], excellent fracture toughness [44,45], good wear resistance [19,46–48], and good corrosion resistance [49,50]. These and other properties were found to be comparable to or better than that of conventional alloys such as stainless steels and nickel superalloys [3,44,51–57]. Figure 2 compares the strength of HEAs and conventional alloys as a function of ductility. The similar strength of both alloy fields can be observed from the figure.

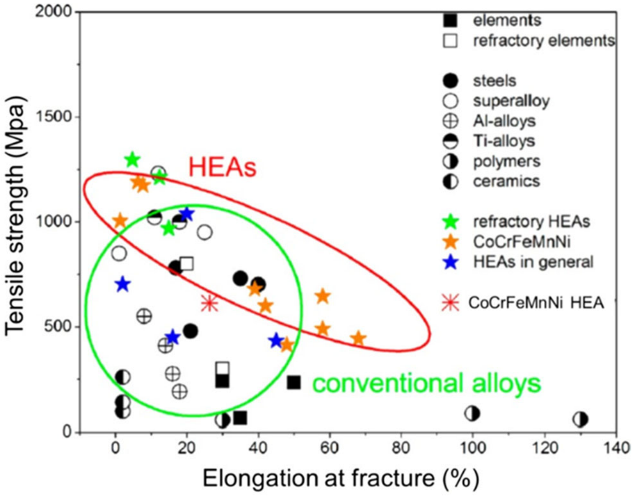

Figure 2: Comparison of tensile properties of conventional alloys and high entropy alloys [58].

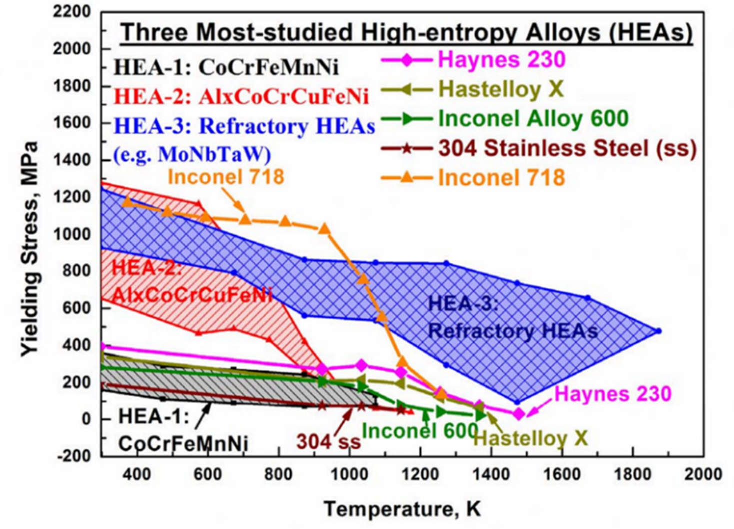

Figure 3: Yield strength as a function of temperature of select conventional alloys and high entropy alloys [54].

Note the general trend of higher strength corresponding to decreased ductility and vice versa. This inverse relationship between strength and ductility, known as the strength-ductility tradeoff, is a phenomenon observed in most metal alloys [6,59]. Strength as a function of temperature is shown in Figure 3. This figure compares different HEAs to five conventional alloys and shows that in the range of cryogenic to high temperature, HEAs have similar or better yield strength compared to the presented conventional alloys. The enhanced properties of HEAs was believed to result from four “core” effects – the cocktail, sluggish diffusion, severe lattice distortion, and entropic stabilization effects [8]. The influence of these has been recently challenged and shown not to be as pronounced as previously thought [10,23]. As research on HEAs continues, a deeper understanding of the four core effects and their influence on HEA properties can be realized.

Considering the ever-increasing number of new HEA discoveries, attempts have been made to group them according to their chemical compositions. The HEA groups include 3d-transition metal HEAs, refractory metal HEAs, transition metals with larger atomic-radius elements, light metal CCAs, lanthanide (4f) transition metal CCAs, brass and bronze CCAs, precious metal CCAs, and interstitial compound CCAs [10,54]. Of the 408 high entropy alloys reviewed by Miracle et al. [10], 85% belong to the 3d-transition metal HEA group which is considered to be analogous to conventional austenitic stainless steels [10,44,55,60–64]. The prototypical 3d-transition metal HEA – equiatomic CoCrFeMnNi alloy – was the first discovered single-phase HEA and has been studied extensively [29,44,56,65–69].

1.2. CoCrFeMnNi High Entropy Alloy

The equiatomic CoCrFeMnNi HEA (known as the Cantor alloy) is a single-phase, disordered solid solution with a face-centered cubic (*fcc*) crystal structure [1,33,70,71]. The alloy's only constituent element possessing a *fcc* crystal structure at room temperature is nickel (Ni). Iron (Fe) and chromium (Cr) both have body-centered cubic (*bcc*) structures, cobalt (Co) has a hexagonal close packed (*hcp*) structure, and manganese (Mn) has a complex *A12* structure [33,66].

Previously believed to be a single-phase solid solution at all temperatures below its solidus [56,70,72], the Cantor alloy has been shown to be metastable and subject to phase decomposition [29,31,60,65,73,74]. Phase decomposition is governed by the diffusion rates of elements which are profoundly influenced by temperature and microstructure

[6,75]. The sluggish diffusion “core” effect of HEAs states that diffusion (atomic motion) in HEAs is relatively slow or hindered. Two studies have shown that diffusion in high entropy alloys is slower when compared to conventional alloys [70,76]; however, the relative decrease in diffusion rate is not very significant [10,23,77]. In the case of the Cantor alloy, all five constituent elements were found to have lower diffusion coefficients than when present in a conventional alloy [60,70]. Tsai et al. [70] found that nickel possesses the lowest diffusion rate and concluded that this element likely controls the Cantor alloy’s overall diffusion process. Elemental diffusion alters the microstructure of alloys and, by extension, influences their mechanical behavior [75].

To the author’s knowledge, six studies [29,31,60,65,73,74] have reported secondary phase formation in CoCrFeMnNi after aging in the intermediate temperature range (450 °C to 900 °C) for 5 min – 12,000 h. According to these studies, nine precipitates can potentially form in the Cantor alloy (summarized in Table 1). Many of these precipitates have been observed at grain boundaries [29,31,60,65,73,74] which are more chemically reactive and have a higher energy state than grain interiors [6]. Due to their relative high energy state, grain boundaries are pathways for atomic diffusion and are preferential nucleation sites for secondary phase formation [29]. Some precipitates resulting from phase decomposition in this alloy are commonly associated with decreased strength, loss of ductility, and premature fracture in conventional alloys [15,29,31,78–80]. For example, Pohl et al. [81] found that formation of the topologically close-packed (*tcp*) σ phase in stainless steel led to embrittlement of the material, reduction in toughness, and loss of corrosion resistance. CoCrFeMnNi is expected to exhibit similar reduced mechanical performance due to phase decomposition. However, the equiatomic composition of the Cantor alloy may result in microstructural and mechanical behavior that differs from that of comparable conventional metals.

Table 1: Summary of secondary phases reported in CoCrFeMnNi high entropy alloy.

Secondary Phase	**Crystal Structure**	**Reference**
Cr phase	*bcc*	[29,31,73,74]
NiMn intermetallic	$L1_0$	[29,31]
FeCo intermetallic	B2	[29,31]
σ phase	*tcp*	[31,65,73,74]
Cr_2MnO_4 oxide	-	[31]
MnS inclusion	-	[31]
$M_{23}C_6$ carbide	-	[31,65]
Cr oxide	-	[60]
Mn oxide	-	[60]

Consider, for example, the corrosion resistance of both the Cantor alloy and stainless steel. Chromium in 300-series stainless steel interacts with the other constituent elements to form a stable passive film that substantially increases corrosion resistance in the alloy. Contrarily, the high manganese content of CoCrFeMnNi impedes the formation of a stable passive surface layer resulting in relatively poor corrosion resistance [82,83]. Other distinguishing characteristics of the Cantor alloy include change in dominant deformation mechanism from dislocation slip at low strain rates to deformation by nano-twinning at high strain rates [10,56,84], and superior mechanical properties at cryogenic temperatures [44].

1.3. Motivation

Materials are assessed for use in practical application by considering their mechanical properties and mechanical behavior. The secondary phases that precipitate in CoCrFeMnNi can have a potentially negative effect on the alloy's mechanical behavior; therefore, it is necessary to understand the mechanical evolution of phase-decomposed CoCrFeMnNi before it can be considered for practical use. Consider, for example, nuclear-generated power – an application where the Cantor alloy could potentially replace or supplement currently used conventional alloys. In pressurized-water reactors (PWRs), 300-series austenitic stainless steels (specifically AISI 304 and AISI 316) are used for piping, steam dryers, pump structures, and structural material for the reactor core [85]. PWRs have an average operating temperature of 345 °C. During a loss of coolant accident (LOCA), the reactor can reach temperatures well beyond 900 °C [86] resulting in ideal conditions for the occurrence of phase decomposition in the Cantor alloy. Presently, the Cantor alloy cannot be assessed for use in this or other applications as secondary phase effects on its mechanical behavior are not sufficiently understood. At the inception of this study, the author was aware of only two reports in literature [29,60] that examined the effects of phase decomposition on the Cantor alloy's mechanical behavior. In the study by He and colleagues [60], dog bone specimens used in low strain rate, elevated temperature tensile experiments were reported to undergo phase decomposition resulting in weakening of the material. Schuh et al. [29] focused on the effects of severe plastic deformation on mechanical properties, microstructure, and thermal stability of the Cantor alloy. The material used in their study was originally coarse-grained but underwent significant grain refinement during plastic deformation resulting in nano-sized grains. After aging at 450 °C for 1 h, secondary phases were observed in the microstructure that led to an increase in strength and loss of ductility. Subsequent aging for 15 h saw reduction in the material's strength. Later studies by Pickering et al. [65] and Otto et al. [31] reported phase decomposition in the Cantor alloy but neither included discussion on mechanical behavior evolution.

This study aims to describe the phase decomposition in coarse-grained equiatomic CoCrFeMnNi after aging 360 h at 610 °C and 720 h at 700 °C, and show how the reported secondary phases influence its mechanical behavior via Vickers microhardness and quasi-static, room temperature tensile experimentation. These mechanical experimentation methods were chosen to maintain consistency with methods reported in literature, making it easier to draw comparisons. The following will provide an overview of the thesis: Chapter 2 introduces and describes the material used in this study as well as the methods employed for heat treating. Chapter 3 describes the methods used for microstructural characterization and mechanical experimentation, and presents the experimental results. Chapter 4 includes discussion of the results. Chapter 5 summarizes the main conclusions of the study. Chapter 6 details possible future work and is followed by the list of references.

Chapter 2. Material and Heat Treatment

2.1. Material

Ingots of CoCrFeMnNi were produced at the National Energy Technology Laboratory (NETL) via induction melting and given a computationally optimized homogenization heat treatment. After solidification, the ingots were hot worked: preheated to 975 °C, forged into rectangular shapes, then rolled into plates with a nominal thickness of 0.16 mm. Following the last roll pass, the plates were reheated for five minutes and then air-cooled [87]. The chemical composition of the Cantor alloy is shown in Table 2 [87]. The presence of interstitial elements – carbon, nitrogen, oxygen, and sulfur – results from normal contamination during fabrication and processing. Their presence is expected to encourage the formation of oxides, nitrides, and carbides during the aging process [55].

Flat dog-bone-shaped specimens with gauge length, width, and thickness measuring 16 mm, 3 mm, and 2 mm, respectively, were made from the Cantor alloy plates using electron discharge machining. A schematic of the dog bone specimen is shown in Figure 4.

Table 2: Chemical composition of CoCrFeMnNi high entropy alloy used in this study [87].

Co wt.%	**Cr** wt.%	**Fe** wt.%	**Mn** wt.%	**Ni** wt.%	**C** ppm	**N** ppm	**O** ppm	**S** ppm
21.47	19.37	18.15	19.6	21.32	274	84	4	13

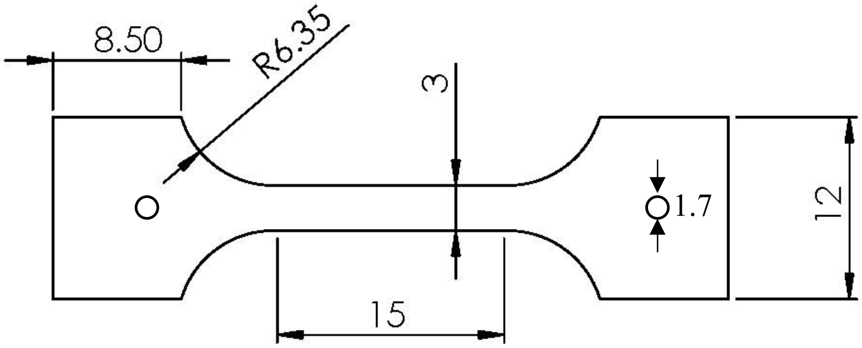

Figure 4: Schematic of dog bone specimen (dimensions in millimeters).

2.1.1. Initial Microstructure

Initial microstructure data for the unaged Cantor alloy is used with permission from colleague Dr. Mitra Shabani [87]. The electron backscatter diffraction (EBSD) inverse pole figure (IPF)-Z map in Figure 5 shows that the unaged Cantor alloy possesses an equiaxed, coarse-grained microstructure with grains that have random crystallographic orientation.

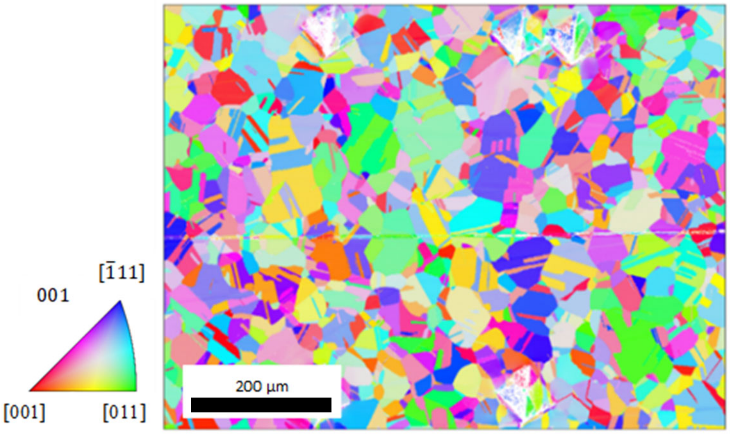

Figure 5: EBSD inverse pole figure (IPF)-Z map created using scanning electron microscope (SEM) [87].

Average grain size of 23.87μm was found using ellipse fitting method in AZtecHKL software [87]. Annealing twins were observed in the microstructure, a common feature of *fcc* metals [88]. EDS maps of the unaged Cantor alloy are shown in Figure 6. There exists no evidence of segregation of any of the five constituent elements, confirming that the Cantor alloy specimens used in this study possess a single phase.

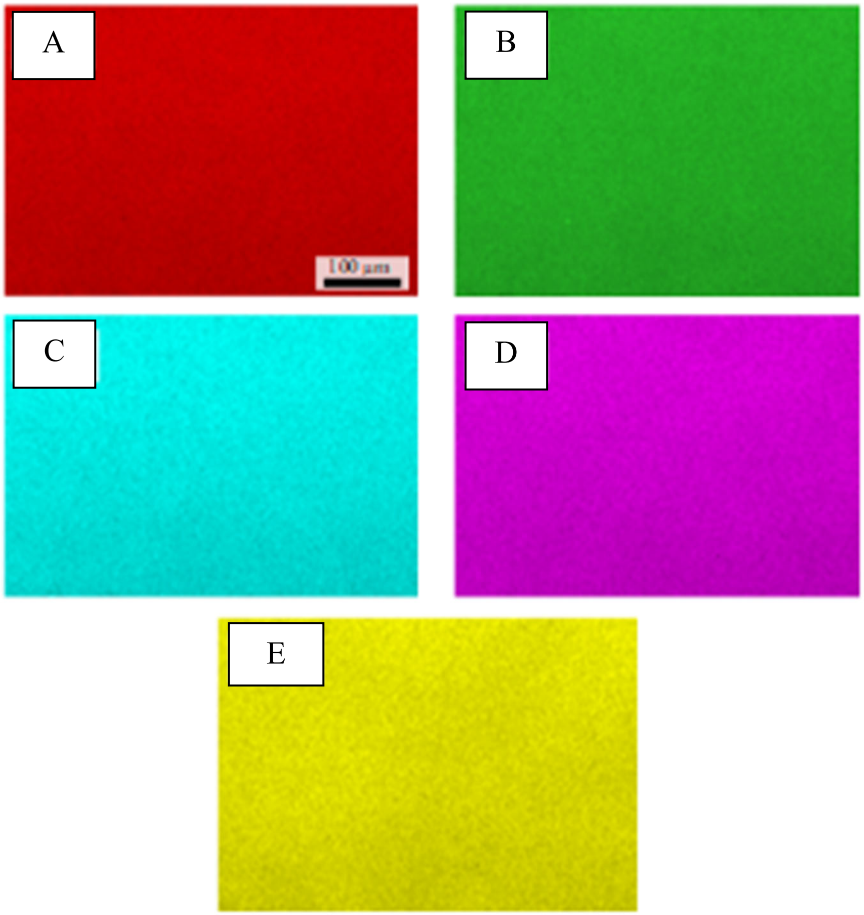

Figure 6: Elemental EDS map of unaged Cantor alloy showing uniform distribution of Cr (a), Fe (b), Co (c), Ni (d), and Mn (e).

2.2. Heat Treatment

Accelerated aging is a type of heat treatment used to more quickly determine long-term material response under certain conditions [89]. In this study, accelerated aging is used to simulate a high temperature environment to induce phase decomposition. Considering time constraints, available equipment, and observations reported in literature [29,31,60,65,73,74], two accelerated aging methods were selected. The short-term aging method is defined in this study as aging for 360 h at 610 °C. The long-term aging method is defined in this study as aging for 720 h at 700 °C. Expected phases for the short-term and long-term aging methods are summarized in Table 3.

Table 3: Accelerated aging methods and expected phases.

Expected Phase	**Phase Crystal Structure**	**Aging Method**	**Reference**
Cr phase	*bcc*	Short-Term (360 h at 610 °C)	[29,31,73,74]
NiMn intermetallic	$L1_0$	Short-Term (360 h at 610 °C)	[29,31]
FeCo intermetallic	B2	Short-Term (360 h at 610 °C)	[29,31]
σ phase	*tcp*	Long-Term (720 h at 700 °C)	[31,65,73,74]

The short-term aging method targets the formation of the Cr phase as well as NiMn and FeCo intermetallics. The long-term aging method targets formation of the σ phase. A phase diagram, created by Saal et al. [90] and based on precipitation phenomena observed by Otto et al. [31], is shown in Figure 7.

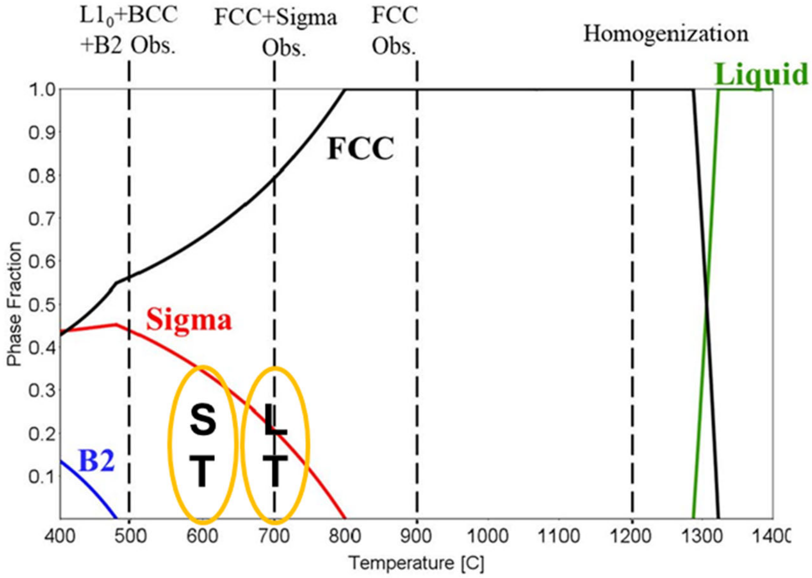

Figure 7: Phase fraction as a function of CALPHAD-predicted temperature [90]. Ovals indicate the area of interest for the short-term (ST) and long-term (LT) aging methods.

Specimens were placed on ceramic plates and carefully set into a Carbolite-Gero Laboratory Chamber Furnace. The furnace featured a primary temperature control and a safety backup control. The backup control was set 75 – 100 °C above the primary control to prevent overheating and reduce the chances of a hazardous event. The heat treatment was timed once the furnace reached target temperature. The specimens were not sealed in tubes during aging. Following heat treatment, laboratory tongs were used to transfer aged specimens from the hot ceramic plate to a cool ceramic plate where they were naturally air quenched for at least 24 h.

Chapter 3. Methods and Results

This chapter includes the presentation of methods and results for microstructural characterization and mechanical experimentation. This is followed by a brief analysis on correlation between strength and hardness results.

3.1. Microstructural Analysis

3.1.1. Microscopy Methods

A Buehler EcoMet™ 3 Grinder-Polisher was used to polish the side of the specimen surface facing the ceramic plate during aging (as opposed to the opposite "airside" surface where significant oxidation damage was anticipated). The Buehler EcoMet™ was first loaded with P400 silicon carbide (SiC) paper and set to rotate at 100 revolutions per minute (RPMs). The specimen was held in place by hand for four minutes, turned 180°, then polished again for four minutes. This technique continued while polishing with P800 and P1200 SiC. For fine polishing (P1500 and P4000), RPM was increased to 200. The specimens were again held in place by hand for four minutes, rotated 180°, and polished once more for four minutes. This method of polishing was also used to prepare specimens for mechanical experimentation.

Specimens were further polished using a standard diamond-paste polishing method for NiCrFe alloys, and their microstructures analyzed for secondary phases by George Wetzel at Clemson University's Advanced Materials Research Laboratory (AMRL). The middle of the specimen surface was scanned using EBSD to produce a map of the microstructure and to analyze the crystal structure of any secondary phases. Energydispersive spectroscopy (EDS) determined the composition of the secondary phases. Elements of interest for EDS included Co, Cr, Fe, Mn, and Ni, as well as contaminant elements O, C, N, and S.

3.1.2. Microscopy Results: Grain Size

EBSD IPF-Z maps of the Cantor alloy aged for 360 h at 610 °C and aged for 720 h at 700 °C are shown in Figures 8 and 9, respectively. The IPF-Z maps for both aged materials show coarse-grained microstructures and the presence of annealing twins. EBSD data was imported into MathWorks® MATLAB® R2020b via the MTEX toolbox for further analysis. A misorientation or tolerance angle and a minimum diameter were specified in the MATLAB® code to define the grains and eliminate noise. The standard Orientation Imaging Microscopy (OIM) Analysis™ misorientation angle of 5° was specified [91,92] for both aged specimens.

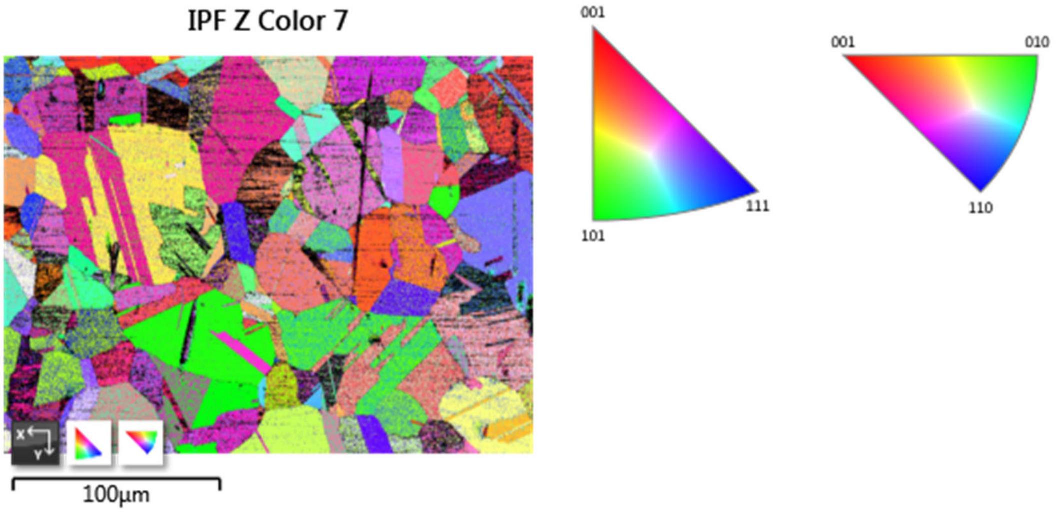

Figure 8: EBSD IPF-Z map of CoCrFeMnNi aged 360 h at 610 °C.

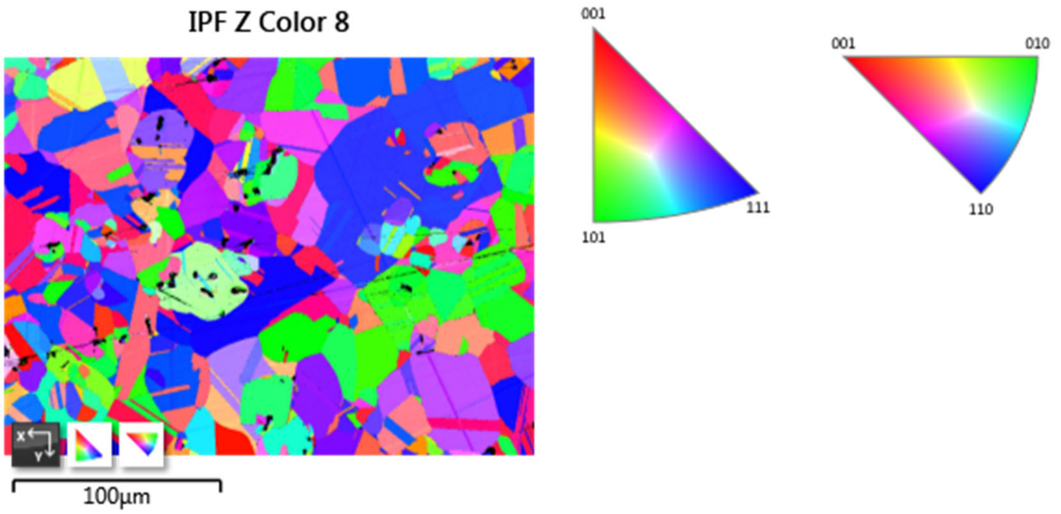

Figure 9: EBSD IPF-Z map of CoCrFeMnNi aged 720 h at 700 °C.

The minimum grain diameter specified for each aged material is based on the respective MTEX EBSD results and takes into consideration the average grain size of the unaged material (23.87µm). The minimum grain diameter was specified as 12µm for the material aged 360 h at 610 °C and 15µm for the material aged 720 h at 700 °C. The average grain size was found to be 24.91µm for the short-term aged material and 24.77µm for the long-term aged material. The lack of substantial grain growth in coarse-grained Cantor alloy following both accelerated aging treatments agrees with observations in literature [31,60,65,73]. Grains grow at elevated temperatures to reduce total boundary energy [6]. The activation energy needed to initiate grain growth in coarse-grained materials is higher than that for fine-grained material. Therefore, only after aging for thousands of hours (e.g. 12,000 h [31]) has substantial grain growth been observed in coarse-grained CoCrFeMnNi.

3.1.3. Microscopy Results: Phase Decomposition

EBSD and EDS images for the material aged 360 h at 610 °C are shown in Figure 10. The backscatter electron (BSE) image (Figure 10a) shows precipitates within grains and at grain boundaries. The precipitates in the grain interiors are most likely oxide, sulfide, or nitride inclusions. Figure 10b-f shows the corresponding EDS maps. The maps show precipitates that are rich in Cr and depleted in all other elements, indicative of a Cr-rich phase. Also present are precipitates rich in Mn and S where a manganese sulfide (MnS) inclusion could be readily assumed. The Cr-rich phase present in this short-term aged material is likely the *bcc* Cr-phase observed in literature, however the EBSD results to explicitly determine the crystal structure of the observed Cr-rich phase were inconclusive. The Cr-rich phase and the MnS inclusions measure roughly 1 – 2μm. There is no evidence of the NiMn and FeCo intermetallics.

Figure 11 shows the microstructure of the material after aging 720 h at 700 °C. Precipitation within grains and at grain boundaries can be seen in the BSE image (Figure 11a). Figures 11b-f show the corresponding EDS maps. There is an increase in the variety of precipitates observed when compared to the short-term aged material. Figure 11e shows significant depletion of Mn with small areas of high Mn concentration. These Mn-rich areas also contain high concentration of sulfur indicating the MnS inclusion.

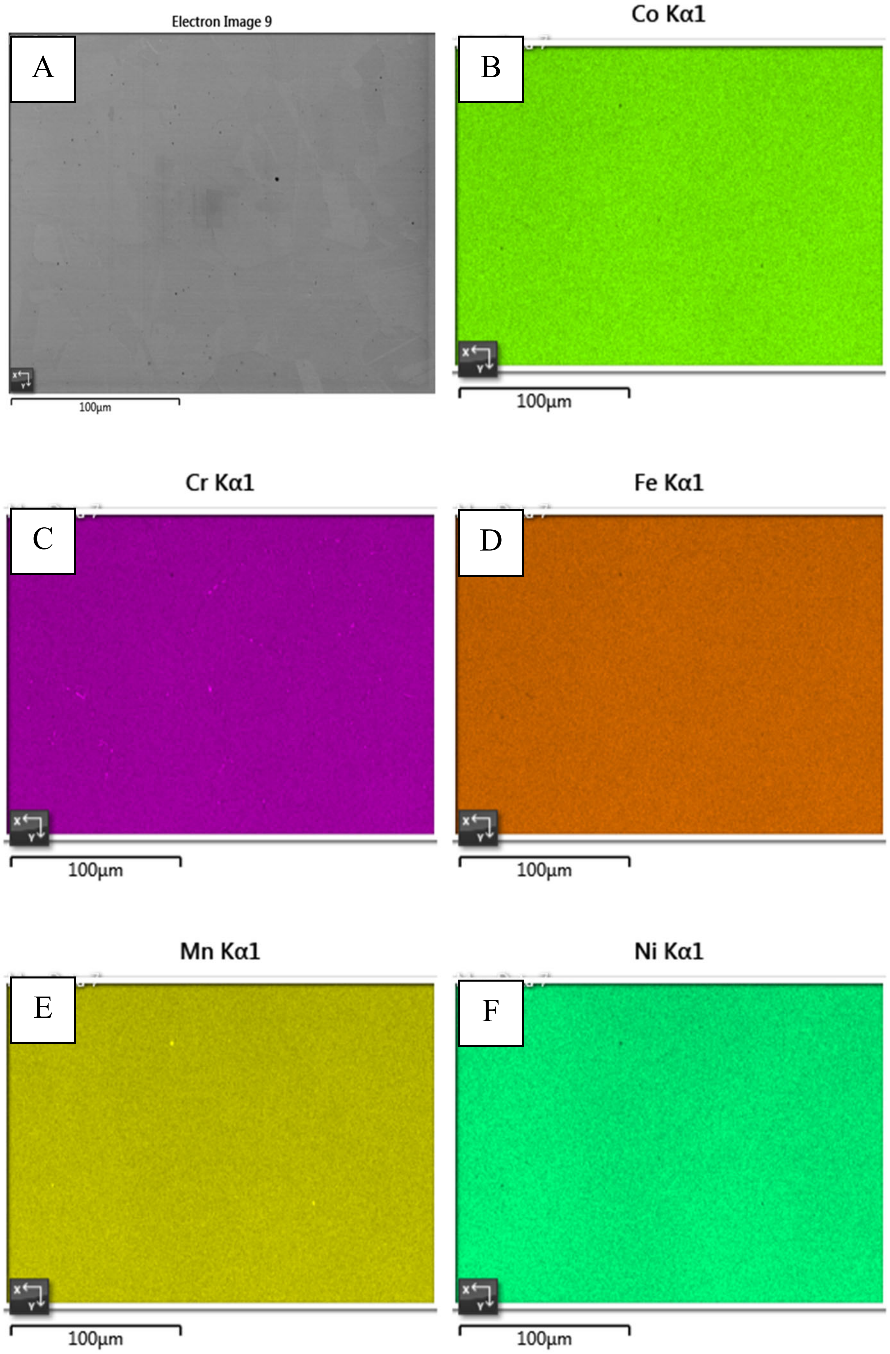

Figure 10: Microstructure of the Cantor alloy aged 360 h at 610 °C. EBSD BSE image (a) and EDS imaging showing distribution of Co (b), Cr (c), Fe (d), Mn (e), and Ni (f). Small Cr-rich phase as well as MnS inclusion can be observed from the images.

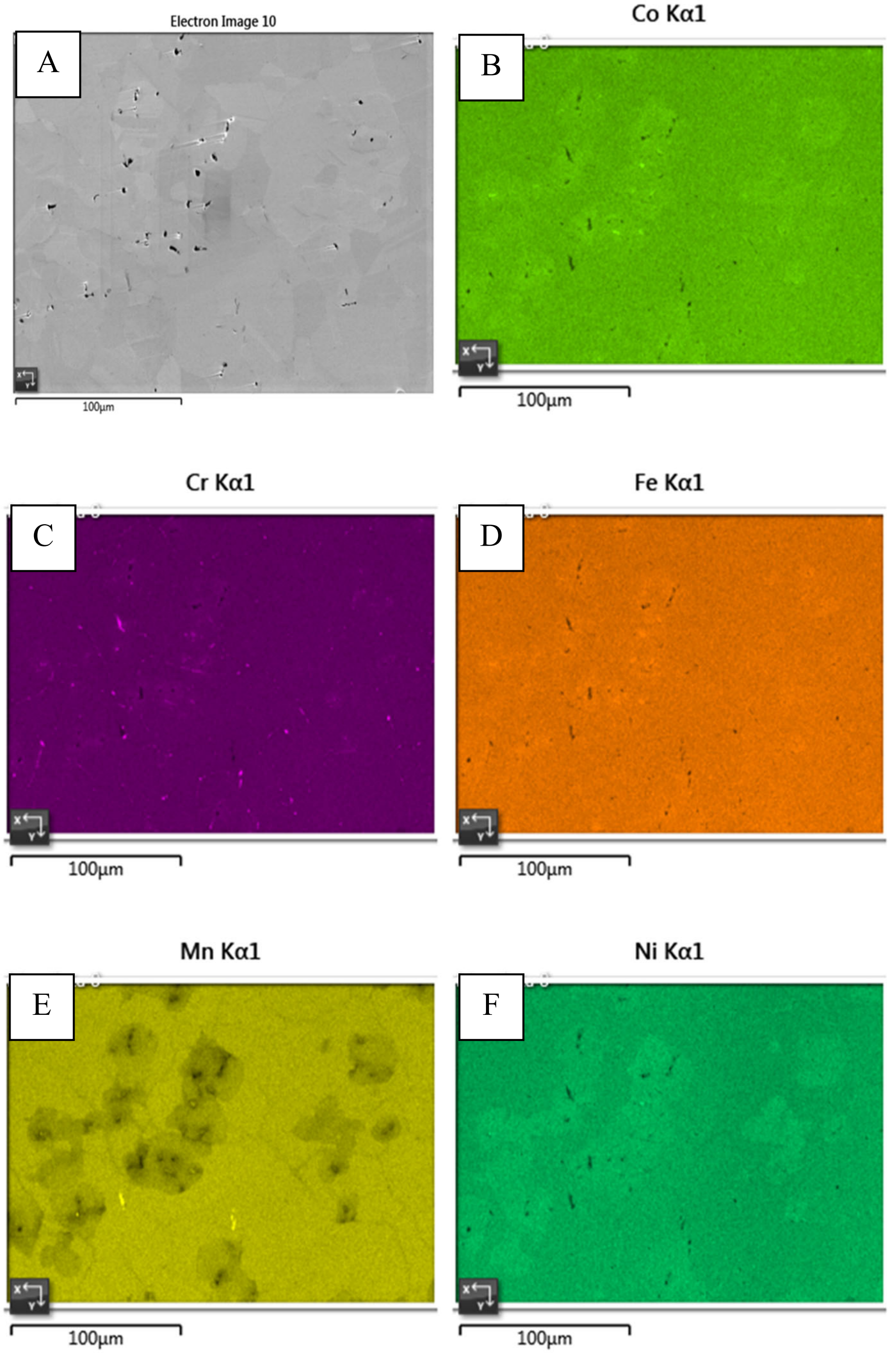

Figure 11: Microstructure of the Cantor alloy aged 720 h at 700 °C. EBSD BSE image (a) and EDS imaging showing distribution of Co (b), Cr (c), Fe (d), Mn (e), and Ni (f). FeCo-rich, FeCr-rich, and Cr-rich phases as well as MnS inclusion can be observed in the images.

Figures 11b and 11d show precipitates rich in Fe and Co indicating the formation of a FeCo-rich phase. In Figure 11c, segregation of Cr can be seen. Some of these Cr-rich areas are shown to be depleted in all other elements, indicative of a Cr-rich phase; others are rich in both Fe and Cr, indicating a FeCr-rich phase and possible nucleation of the σ phase. Figure 11f shows areas of relatively high nickel concentration. The Cr-rich and FeCo-rich phases present in this long-term aged material are likely the *bcc* Cr phase and B2-FeCo intermetallic, respectively. However, the EBSD results to explicitly determine the crystal structure of the Cr-rich and FeCo-rich phases, as well as the FeCr-rich phase, were inconclusive.

3.2. Microhardness Experimentation

3.2.1. Microhardness Methods

A Leco MHT Series 200 was used to conduct Vickers microhardness experiments. Specimens were loaded with a force of 1000 gf at a dwell time of 15 seconds [29]. Each experiment consisted of ten indentations [71] measured with an onboard filar-scale micrometer. To eliminate the interaction of stress fields created by indenting the specimen surface, subsequent indents were spaced at 10x the average diameter of the previous indent, measured in filar units. This spacing method was suggested in the Leco MHT Series 200 device manual and continued until reaching any edge. Figure 12 shows Cantor alloy with indents denoted by colored diamonds. The indentations marked here are not to scale.

Figure 12: Cantor alloy specimen used for microhardness experiments. Indents denoted by colored diamonds (not to scale).

Jae Lowe of the Clemson University Materials Science and Engineering Department assisted in verifying the measurement error of the Leco 200's micrometer. It was determined that one filar unit was equivalent to 0.02428 mm. This value was used to convert the measured diameters of the indents from filar units to millimeters. Following conversion, the average diameter ($d_{average}$) was found for each indent. To determine the Vickers hardness number (HV), $d_{average}$ was input into Equation (4), where P is the load in kg [6].

$$HV = \frac{1.854P}{d_{average}^{2}} \tag{4}$$

3.2.2. Microhardness Results

Vickers microhardness was used to estimate the effects of aging on the strength of the CoCrFeMnNi specimens. Based on select studies from literature, the hardness of the unaged Cantor alloy ranges between 144 HV [93] and 176 HV [94]. Results from microhardness experimentation, summarized in Table 4, are within the range given in literature, and are also comparable to 304 stainless steel and 316 stainless steel [95]. A value of 147 HV was recorded for the unaged Cantor alloy with a standard deviation of ± 3 HV. A slightly decreased hardness of 146 HV was recorded for the Cantor alloy aged

360 h at 610 °C with a standard deviation of ± 2 HV. A slightly higher value of 152 HV was recorded for the Cantor alloy aged 720 h at 700 °C with a standard deviation of ± 3 HV. Statistical significance calculations for the hardness magnitudes of the short-term and long-term aged materials are summarized in Table 5. The Z score was calculate using Equation (5) where X is the hardness of the unaged material and μ is the average hardness of the aged material.

$$Z = \frac{X - \mu}{standard\ deviation} \tag{5}$$

Table 4: Results of Vickers microhardness experimentation

Material	**Aging Method**	**Average Hardness (HV)**	**Standard Deviation (HV)**	**Percent Change Compared to Unaged Cantor Alloy**
Cantor Alloy	Unaged	147	± 3	-
Cantor Alloy	360 h at 610 °C	146	± 2	-1%
Cantor Alloy	720 h at 700 °C	152	± 2	+3%
304 Stainless Steel	-	129	-	-12%
316N Stainless Steel	-	155	-	+5%

Table 5: Statistical significance of the hardness of the aged materials.

Aging Method	**Average Hardness (HV)**	**Z score**	**P-value**	**Statistically Significant**
360 h at 610 °C	146	0.5	0.6170	No
720 h at 700 °C	152	-3.0	0.0027	Yes

The Z score was then converted to p-value via a calculator tool. The significance level, α, was taken to be 5%, meaning the p-value of the data must not exceed 0.05 to be considered significant. It was found that the hardness of the short-term aged material was statistically insignificant, and the hardness of the long-term aged material was statistically significant.

3.3. Tensile Experimentation

3.3.1. Tensile Experimentation Methods

Digital image correlation (DIC) was used in conjunction with tensile experimentation to determine the mechanical behavior of the aged dog bone specimens. DIC is a non-contact, optical technique used in this study to estimate 2D displacements via a sequence of images taken of the specimen surface during tensile testing. From a reference image (e.g. the first image), subsequent images are matched or correlated to calculate strain. This technique requires the specimen surface be covered with a speckled pattern.

The size of the speckles, their contrast, and distribution, etc. are important for successful image correlation and noise reduction [96]. After polishing, the Cantor alloy specimens were speckled using an air brush and white paint, and then loaded into an MTS Landmark 370 hydraulic load frame. Small metal clamps and #51 pins, at top and bottom of the specimen (see Figure 4), were used to hold the specimen in place and maintain alignment. Uniaxial, quasi-static, room temperature tensile experiments were conducted at a strain rate of 1 x 10^{-4} mm/mm until specimen failure. Figure 13 shows the setup of the load frame with a specimen held via hydraulic grips and the DIC camera setup including cameras and light source.

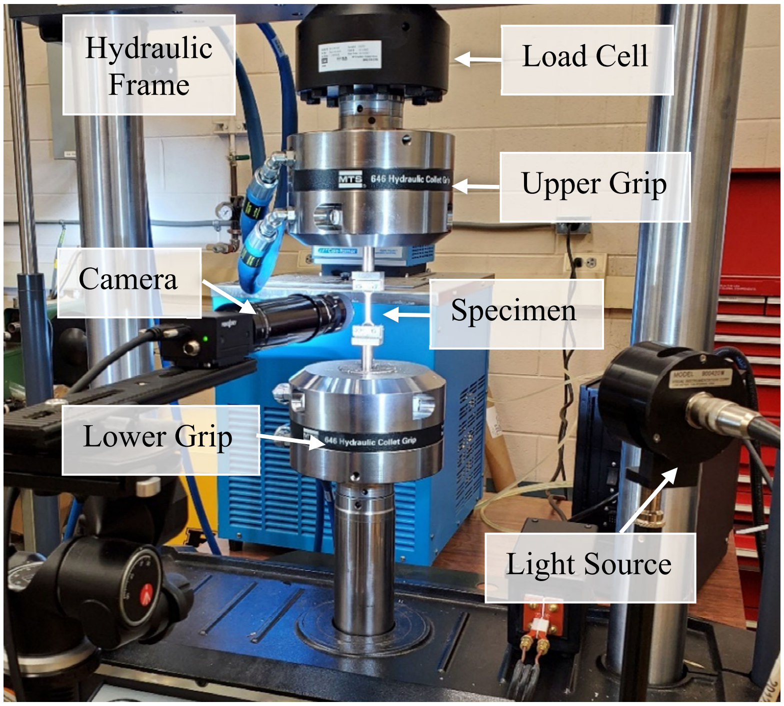

Figure 13: MTS load frame and camera setup.

A Point Grey GS3 camera with 1x Navitar adapter lens was used to capture images during the tensile experiments. The images were correlated via the VIC-2D 6 application using partitioned correlation method. Partitioned correlation can be used as an alternative method when the images captured during a test cannot be correlated back to a single reference image; or when the summation of error, as done in incremental correlation, is not ideal. When correlating using partitioned correlation, images are divided into multiple sub-series where each image in a sub-series is correlated back to the starting image of that sub-series. Images were analyzed in VIC 2D 6 using the following user-parameters for each specimen: step size (ST) of 5, strain computation filter size (SW) of 5, and subset size (SZ) of 29 px. Each pixel within a subset was center-weighted using Gaussian weights to achieve the best combination of spatial resolution (SR) and displacement resolution. The virtual strain gauge size (VSG), calculated using Equation (6), was found to be 21 px. The spatial resolution, calculated using Equation (7), was found to be 49 px.

$$VSG = \big(ST * (SW - 1)\big) + 1 \tag{6}$$

$$SR = \big(ST * (SW - 1)\big) + SZ \tag{7}$$

VIC-2D 6 uses a subset shape function method to calculate Lagrangian strains. Figure 14 is an image obtained from VIC 2D 6 showing the Cantor alloy specimen subjected to tensile forces. Once strain values are obtained for the images in the initial sub-series, total strain is calculated by adding the strain value of the last image in the initial sub-series to the strain value of each image in the subsequent sub-series.

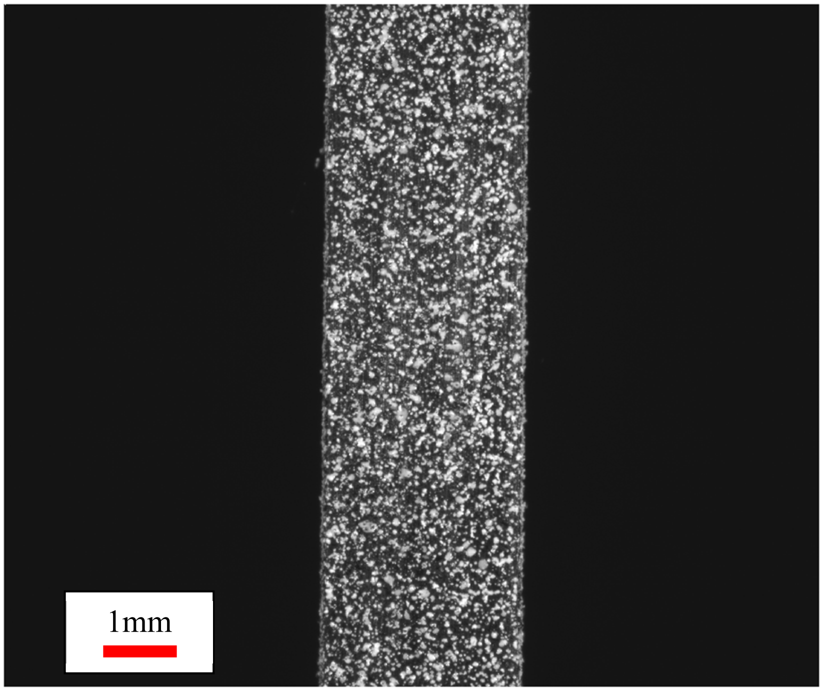

Figure 14: Image of Cantor alloy specimen under tension viewed in VIC-2D 6.

3.3.2. Tensile Experimentation Results

Stress-strain curves obtained from tensile experimentation of the unaged and aged material are summarized in Figure 15; the elastic region is shown in Figure 16. The strain energy density, or toughness (U_t), represented by the area under a stress-strain curve, was calculated for the Cantor alloy specimens using MathWorks® MATLAB®. Area reduction, AR, was calculated by taking the percent change of the cross-sectional area before (A_0) and after (A) tensile experimentation The area reduction formula is shown in Equation 8.

$$AR = \frac{A_0 - A}{A_0} \tag{8}$$

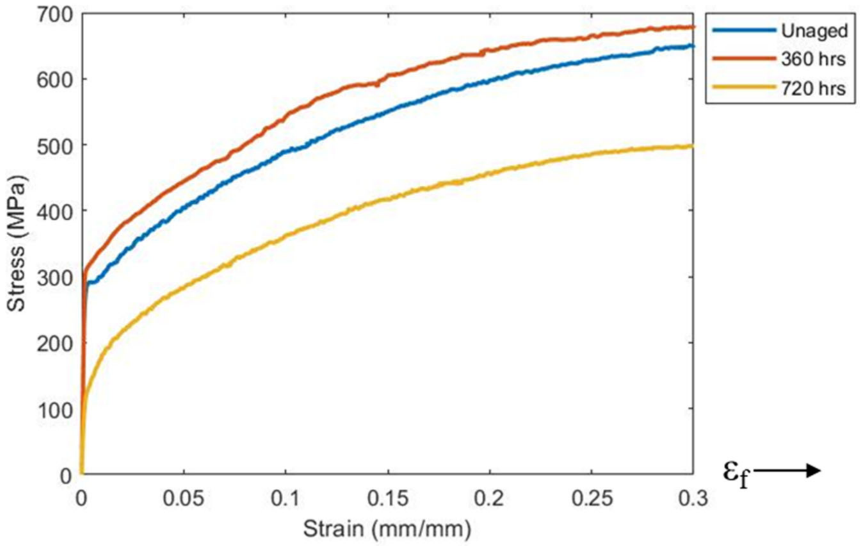

Figure 15: Stress-strain curves of unaged and aged Cantor alloy. Note that strain to failure is not displayed in the graphic.

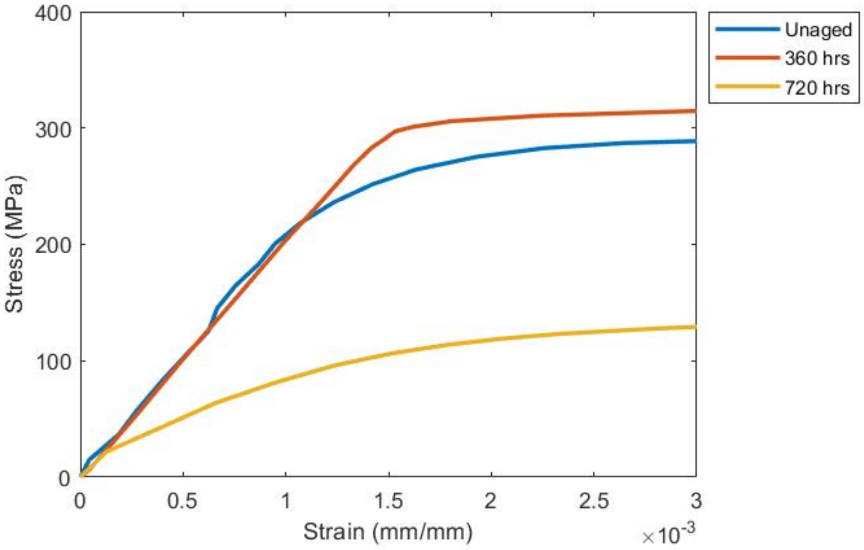

Figure 16: Elastic region of the stress-strain curves of unaged and aged Cantor alloy.

The gauge thickness and gauge width used to calculate *A* were both measured at the point of specimen failure. Select tensile results for the Cantor alloy, as well as tensile data for 304 and 316 austenitic stainless steel [55], are shown in Table 6.

The strength of unaged Cantor alloy measured 291 MPa and 657 MPa for 0.2% offset yield strength (YS) and ultimate tensile strength (UTS), respectively, which are within the range of reported values in literature [54,56,57,87,94]. Area reduction of the unaged Cantor alloy measured 54% and the alloy's toughness measured 170 J/m^3. After aging 360 h at 610 °C, YS increased by 9% to 319 MPa and UTS rose 3.5% to 680 MPa. Area reduction remained largely similar to that of the unaged Cantor alloy, decreasing by only 1%. The toughness of the material increased to 173 J/m^3.

After aging 720 h at 700 °C, the material exhibited decreases in strength, ductility, and toughness. YS of the longer aged Cantor alloy degraded by 55% to 130 MPa and the UTS fell 23% to 505 MPa. Area reduction and material toughness decreased to 46% and 168 J/m^3, respectively.

Table 6: Results of tensile experimentation

Material	**Aging Method**	**0.2% Yield Strength (MPa)**	**UTS (MPa)**	**Area Reduction**	**Elongation**	**Phases Observed**
Cantor Alloy	Unaged	291	657	55%	-	-
Cantor Alloy	360 h at 610 °C	319	680	54%	-	Cr MnS
Cantor Alloy	720 h at 700 °C	130	505	46%	-	FeCo FeCr Cr
304 Stainless Steel	**-**	205	515	-	40%	-
316N Stainless Steel	**-**	240	550	-	30%	-

3.4. Correlation Between Strength and Hardness

Yield strength and hardness are measures of a material's resistance to plastic deformation [6]. The relationship between these material properties is approximated by Equation (9) where HV is the Vickers hardness number and σ_y is the yield strength of the material [97,98].

$$HV = 3\sigma_y \tag{9}$$

This relationship was established via analysis of slip-line field of indentation by Tabor [97] and analysis of the five triangular portions of tested materials by Ashby et al. [98]. Other studies report a similar relationship between the ultimate tensile strength (UTS) and hardness [19], [20], as shown in Equation (10), where HV is the Vickers hardness number and σ_{UTS} is the ultimate tensile strength of the material.

$$HV = 3\sigma_{UTS} \tag{10}$$

Tabor [97] and Ashby et al. [98] noted that this relationship is only valid for materials that do not exhibit work-hardening behavior [99]. For work-hardening materials such as the Cantor alloy [55–57,84,100], the hardness-to-strength constant, K, would not be equal to 3, but instead would have to be found experimentally [101]. To this end, the Vickers microhardness numbers for the unaged and aged Cantor alloy were converted to units of MPa using Equation (11) [6].

$$Hardness\ (MPa) = 9.807HV \tag{11}$$

K_y was then calculated by taking the quotient of the hardness (MPa) and yield strength. K_{UTS} was similarly calculated by dividing the hardness (MPa) by the UTS. The K_y and K_{UTS} values are included in Tables 7 and 8, respectively.

Table 7: Correlation between yield strength and hardness.

Material	**Average Hardness (HV)**	**Hardness (MPa)**	**0.2% Yield Strength (MPa)**	**K_y**
Unaged	147	1441.6	291	4.9
Short-Term Aged	146	1431.8	319	4.5
Long-Term Aged	152	1490.6	130	11.5

Table 8: Correlation between ultimate tensile strength and hardness.

Material	Average Hardness (HV)	Hardness (MPa)	UTS (MPa)	K_{UTS}
Unaged	147	1441.6	657	2.2
Short-Term Aged	146	1431.8	680	2.1
Long-Term Aged	152	1490.6	505	2.9

The hardness-to-strength constant is affected by yield stress, the material's work hardening exponent, and residual stress [101]. The tensile experimentation results show that phase decomposition significantly impacts the yield stress. Residual stress can be induced by heat treatment and mechanical processing [101]. The Cantor alloy specimens used in this study were subjected to homogenization heat treatments at 975 °C and mechanically processed via hot-working. The material underwent further mechanical processing when the dog bone specimens were machined from the flat plates and underwent further heat treatment during accelerated aging. The residual stresses incurred during processing and heat treating of the Cantor alloy, as well as its work-hardening ability, all contribute to the variances in K_y and K_{UTS}. Moreover, these factors also explain why the K values presented in Tables 7 and 8 are not equal to the original constant of 3 reported by Tabor [97] and Ashby et al. [98]. The relationship between strength and hardness is difficult to apply in this case, where the material has a residual stress distribution induced by processing and heat treating and exhibits work-hardening during plastic deformation.

Chapter 4. Discussion

4.1. Material Response After Short-Term Aging

Aging CoCrFeMnNi for 360 h at 610 °C resulted in precipitation of a Cr-rich phase and MnS inclusion, which agrees with observations from literature [29,31,60,73,74]. The interstitial elements C, N, O, and S diffuse more rapidly than elements of the host Cantor alloy [31,102,103] – where Mn has the fastest diffusion rate followed by Cr, Fe, Co, and Ni [70]. Considering the diffusivities of the elements, it can be concluded that MnS formed before the Cr-rich phase, and that B2-FeCo would have precipitated given a longer aging time. The nucleation of $L1_0$-NiMn was primarily hindered by the slow diffusion of Ni.

Manganese sulfide is the predominant inclusion formed during solidification of steel [104], and it appears to readily form in the Cantor alloy based on the results presented in this thesis and in the study by Otto et al. [31]. Segregated Cr is the most frequently reported precipitate in phase-decomposed Cantor alloy [29,31,60,73,74]. It is known that nitrogen destabilizes the microstructure of AISI 304 stainless steel and promotes segregation of Cr [103]. Therefore, in addition to relatively fast diffusion of Cr, precipitation of the Cr-rich phase in short-term aged CoCrFeMnNi was likely promoted by the contaminating nitrogen.

The presence of the Cr-rich phase and MnS inclusion did not significantly affect the material hardness after aging 360 h at 610 °C. Pure Cr, with a hardness of 90 HV [105], is softer than the unaged Cantor alloy suggesting that a large volume fraction of segregated chromium would decrease the overall hardness of the host alloy. At the time of this writing, no explicit hardness data could be found for the Cr phase in literature. As such, care is taken to not substitute the hardness of pure Cr for that of the observed Cr-rich phase. Klimova et al. [74] found that the *bcc* Cr phase in conjunction with the σ phase increased the hardness of their aged Cantor alloy. MnS has a hardness of 170 HV [106], which is greater in magnitude than that of unaged CoCrFeMnNi. Since the hardness of the short-term aged Cantor alloy is statistically similar to that of the unaged material (Tables 4 and 5), it can be concluded that the volume fraction of the MnS and Cr-rich precipitates was too small to have any significant impact on the overall hardness.

The increase in yield strength after short-term aging can be attributed to formation of the Cr-rich phase [74] resulting in precipitation strengthening. The formation of this secondary phase distorted the host *fcc* lattice, generating lattice strains at the precipitate-matrix interface [6]. During plastic deformation, these distortions strengthened the alloy by impeding dislocation slip [6], which is the dominant deformation mechanism in the Cantor alloy [56,87] (similar to other *fcc* metals and metal alloys [10,47,56,107–112], and stainless steels [110,113–116]). The increase in UTS can be attributed both to phase decomposition as well as extensive work hardening. Work hardening during tensile deformation is also observed in 300 series austenitic stainless steel [55–57,87,100]. However, the Cantor alloy exhibits superior work hardening at the onset of plastic deformation [117] when compared to austenitic stainless steel at room temperature [44,118]. This is due to the Cantor alloy having a high hardening coefficient of 677 MPa $\mu m^{-0.5}$ [71]. Comparatively, the hardening coefficient of most conventional *fcc* metals does not exceed 600 MPa $\mu m^{-0.5}$ [119]. The presence of MnS has been shown to have negligible effect on the yield strength, ultimate tensile strength, and work hardening of steel when the material is subjected to longitudinal forces [120]; the same can be concluded for the short-term aged Cantor alloy, especially considering its small volume fraction.

The ductility of the short-term aged Cantor alloy only decreased by 1%, though the 9% increase in strength from 291 MPa to 319 MPa was not overly large. Sulfur and MnS are known to negatively impact the ductility of steel [104,106,120], but their small volume fractions had negligible effect. It is apparent that aging the Cantor alloy 360 h at 610 °C achieves a delicate balance between strengthening and ductility degradation with a 9% increase in yield strength and no significant loss in ductility. Though these results are promising, the corresponding aging parameters should be considered as a maximum and not as safe service conditions. Any increase in aging time or temperature will likely result in softening and substantial weakening of the material based on observations reported in literature [29,60,74,121].

4.2. Material Response After Long-Term Aging

After aging 720 h at 700 °C, precipitation of Cr-rich, FeCo-rich, and FeCr-rich phases as well as the MnS inclusion were observed. The volume fractions of the Cr-rich phase and MnS inclusions were noticeably larger than those observed for the short-term aged material. Increase in volume fraction with longer aging time is consistent with observations by Schuh et al. [29] and Klimova et al. [74]. The relationship between volume fraction and time is explained in part by the second law of thermodynamics: given sufficient time, the volume fraction of phases will continue to evolve until the equilibrium state is reached [6,9,16,61,122]. Volume fractions also increase with increasing temperature due to the temperature dependence of diffusion-related processes [71,74]. Change in phase volume fraction with time and temperature is also affected by several other factors including phase nucleation and growth rates, density and distribution of nucleation sites, and the pinning effect of adjacent precipitates [61]. The widespread presence of the Cr-rich phase in conjunction with the FeCr-rich phase in this long-term aged material is indicative of a metastable condition. Praveen et al. [24] developed a phase diagram of equiatomic CoCrFeMnNi (Figure 17) showing that increase in FeCr volume fraction coincides with decrease in Cr phase volume fraction, similar to another observation from literature [74].

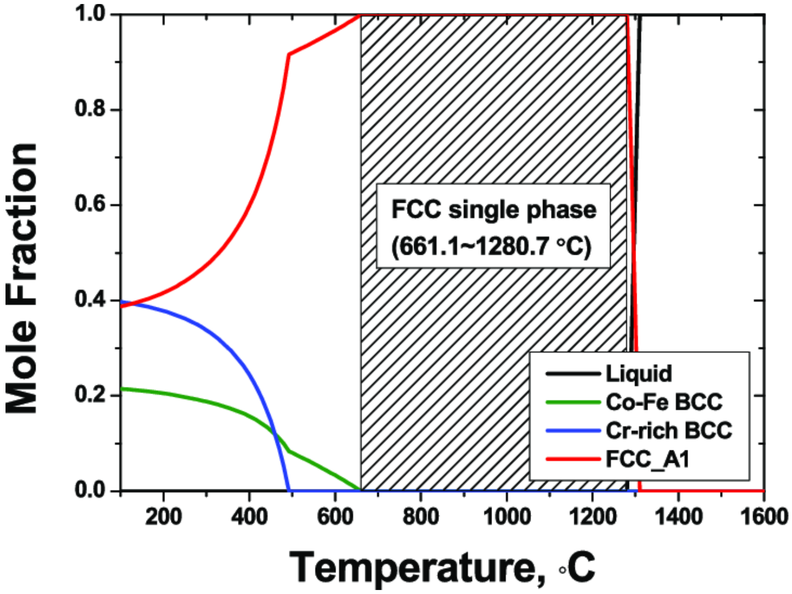

Figure 17: Phase diagram of equiatomic CoCrFeMnNi [24].

The diffusion rates of the elements suggest that the MnS inclusion formed first followed by the Cr-rich phase, FeCr-rich phase, and finally FeCo-rich phase. Attempts were made to fully characterize the FeCr-rich precipitates using EBSD, but those results were inconclusive. The σ phase is a FeCr-rich compound [123] known to readily precipitate in ferrite (*bcc*-structured iron) which is stabilized by chromium [80,124,125]. However, iron in equiatomic CoCrFeMnNi is austenitic (*fcc*-structured), and precipitation of the σ phase occurs about 100 times slower in austenite than in ferrite [80]. The austenite to σ transformation in stainless steel takes thousands of hours to occur due to incoherent boundaries between austenitic iron and σ phase, making nucleation of the latter more difficult [80]. The FeCr-rich areas observed in the microstructure of the long-term aged Cantor alloy also exhibit relatively high concentrations of Co and Ni which stabilize austenite (Mn, N, and C are also austenite stabilizers) [124,125]. Therefore, it can be deduced that the austenite-stabilizing elements in CoCrFeMnNi (including the contaminant elements) actively slowed the formation of σ phase making its precipitation quite difficult. On the other hand, ferrite can form temporarily during aging. In this case, the σ phase will precipitate relatively quickly via the ferrite [80]. Microscopy methods, such as EBSD, could have identified iron transformation, however, none were conducted due to limitations in time and equipment. Though the σ phase is made up of iron and chromium, it is important to note that the presence of FeCr-rich precipitates do not explicitly indicate precipitation of the σ phase; rather, segregation of Fe and Cr is a precursor to σ phase formation [80,123,126].

The hardness of long-term aged Cantor alloy is 3% higher in magnitude than unaged Cantor alloy (Table 4). FeCo and FeCr are hard intermetallic phases that would contribute to a significant increase in hardness [29,31,35,65]. Conversely, segregation of

Ni causes local softening due to localized reduction of stacking fault energy (SFE) [121]. This results in alternating hard and soft regions throughout the material, explaining the marginal increase in hardness despite the significant presence of hard intermetallic phases.

The substantial decrease in yield strength from 224 MPa to 105 MPa can be attributed directly to phase decomposition. For precipitates to strengthen an alloy, their volume fraction must be precisely controlled [6]; otherwise, they result in significant degradation of material properties. This is known as overaging. Precipitation strengthening of a material increases with aging time until reaching a maximum, after which the strength decreases [6]. In this study, the precipitate size and assortment of secondary phases contributed to the detrimental decline in yield strength. The UTS exhibited a shallower decline due in part to strength preservation via the Cantor alloy's extensive work hardening ability. The significant decrease in strength was not accompanied by an increase in ductility. In fact, the long-term aged material exhibited significant reduction in ductility. This is due to the overall brittle nature of the secondary phases in the phase decomposed microstructure, and severe softening resulting from segregation of Ni. The effects of phase decomposition on the mechanical properties of long-term aged Cantor alloy are consistent with reports concerning phase decomposed austenitic stainless steel, namely degradation in the material's strength and ductility [123].

4.3. Application Consideration

PWRs have an average operating temperature of 345 °C. At this temperature, there is virtually no risk of phase decomposition in the Cantor alloy. During a loss of coolant accident (LOCA), the reactor will exceed this temperature, reaching well beyond 900 °C. Realistically, LOCA will not persist for more than a few hours before either the incident is corrected or total meltdown occurs [86]. If reactor temperatures are allowed to persist at the conditions of the short-term aging method (360 h at 610 °C), results from the present study show that the Cantor alloy will undergo precipitation strengthening with no significant loss in ductility. If reactor temperatures are allowed to persist at the conditions of the long-term aging method (720 h at 700 °C), results from the present study show that the potential for precipitation of more detrimental phases increases in the Cantor alloy. However, the extent of phase decomposition is time dependent and the nucleation and growth of these phases would be insignificant given the timeline of a realistic loss of coolant accident. Furthermore, Chen et al. [127] recently reported that the Cantor alloy is resistant to radiation, meaning that irradiation has virtually no effect on its mechanical behavior. Based strictly on comparable strength, LOCA timeline and temperature ranges, and phase decomposition results presented in this thesis as well as the literature [29,31,60,65,73,74,127], it can be concluded that the Cantor alloy is indeed a viable candidate material to replace or supplement the conventional alloys used in this application.

Accelerated aging is a powerful tool that extends beyond the simulation of a high temperature environment. Other factors that can be simulated include radiation, humidity, and temperature cycling [89]. By including these and other factors that may be expected in a nuclear reactor application, long-term investigations on the behavior/stability of the Cantor alloy can be conducted.

Chapter 5. Conclusions

Aging CoCrFeMnNi for 360 h at 610 °C resulted in precipitation of a Cr-rich phase and MnS inclusion. The hardness of the short-term aged Cantor alloy (146 HV) was statistically similar to that of the unaged material, indicating that the Cr-rich phase and MnS precipitates were too small to significantly affect the material hardness. The short-term aged material was precipitation strengthened via formation of the Cr-rich phase which distorted the host *fcc* lattice and impeded dislocation slip. The increase in UTS is attributed both to phase decomposition as well as the extensive work hardening capabilities of the Cantor alloy. Overall, a delicate balance between strengthening and ductility degradation was achieved in the short-term aged alloy with a 9% increase in yield strength and no significant loss in ductility.

After aging 720 h at 700 °C, precipitation of Cr-rich, FeCo-rich, and FeCr-rich phases as well as the MnS inclusion were observed. The volume fractions of the Cr-rich phase and MnS inclusions were noticeably larger than those observed for the short-term aged material. The long-term aged material exhibited alternating hard and soft regions resulting in an overall hardness 3% higher in magnitude than unaged Cantor alloy. A substantial decrease in yield strength from 224 MPa to 105 MPa was observed. The UTS exhibited a shallower decline due in part to strength preservation via the Cantor alloy’s extensive work hardening ability. The significant decrease in strength was accompanied by significant reduction in ductility due to the overall brittle nature of the secondary phases and severe softening resulting from segregation of Ni. The effects of phase decomposition on the mechanical properties of long-term aged Cantor alloy are consistent with reports concerning phase decomposed austenitic stainless steel, namely degradation in the material’s strength and ductility.

Chapter 6. Future Work

In this study, it was shown that aging Cantor alloy 360 h at 610 °C results in precipitation hardening due to phase decomposition. Aging the alloy for longer times and at higher temperatures resulted in overaging and subsequent weakening. Of the four studies in literature that include mechanical testing of phase decomposed CoCrFeMnNi [29,60,74,121], only the two most recent studies [74,121] were primarily aimed at investigating the effects of phase decomposition on the material. More intentional studies should be carried out to gain a wholistic understanding of the relationship between phase decomposition and mechanical properties of the Cantor alloy.

Beyond the present research, there are microstructural factors that should be systematically investigated – including initial composition, initial grain size, fabrication methods, and other deformation prior to aging – to determine their influence on phase decomposition. For example, the NiMn phase is reported to form in hot-worked Cantor alloy with grain size of 1mm and contaminating sulfur and carbon after aging 12,000 h at 500 °C [31]. In a cold-worked, contaminant-free Cantor alloy specimen consisting of 50nm-sized grains and subjected to prior severe plastic deformation, the NiMn phase formed at 450 °C after just 5 min [29]. In the present study, where hot-worked, coarse-grained Cantor alloy contaminated with O, N, S, and C was aged for 360 h at 610 °C and 720 h at 700 °C, the NiMn phase was not observed at all. A possible future study would involve systematic analyses of multiple Cantor alloy specimens aged at the same heat treating parameters while the initial composition, initial grain size, fabrication method, or other prior deformation is allowed to vary one at a time. Heat treatment temperatures of interest include any of the temperatures in the intermediate temperature range (450 °C to 900 °C), not already reported in literature [29,31,60,65,73,74], where the Cantor alloy is known to be metastable and phase decompose including but not limited to 550, 575, 650, 675 °C, etc. Conducting studies, even at these intermediary temperatures, will ensure the availability of any necessary data on the conditions required to induce phase decomposition in the Cantor alloy. Possible variances in initial composition include the use of a contaminant-free and contaminated Cantor alloy control. It is shown in the studies by He et al. [60] and Otto et al. [31], as well as in the present study, that the presence of contaminants can impact phase decomposition. In exploring different grain sizes, sizes of interest would include ultrafine, nanocrystalline grains (50nm or less) [29], medium coarse-grains (1 – 20μm) [60,74], and coarse-grains (1mm or larger) [31]. Grain size is known to affect the strength of materials [71] and their deformation mechanisms [128]; and phase decomposition preferentially occurs at grain boundaries in the Cantor alloy [29,31,60,65,73,74]. Smaller grains usually correspond to higher strength and more grain boundaries when compared to materials with larger grains [6]. Variance in fabrication method would involve a selected hot working process and a cold working process. Hattestrand et al. [129] found that cold working does in fact influence the phase decomposition in duplex stainless steel. Variance in prior deformation could include a prior deformed and unperturbed Cantor alloy control. He et al. [60] and Schuh et al. [29] both report phase decomposition after deformation of the Cantor alloy, albeit under differing testing parameters. By performing a study in the manners described, the specific microstructural factor (initial composition, initial grain size, fabrication method, or other prior deformation) can be isolated and its influence on the occurring phases can be explored.

A second consideration is to increase the strain rate used in tensile experimentation. The dominant deformation mechanism in the Cantor alloy is known to change from dislocation slip at low strain rates to deformation via nano-twinning at dynamic strain rates [10,56,84]. Only two reports have conducted dynamic strain rate mechanical experimentation (one in tension [60] and one in compression [121]) of phase decomposed Cantor alloy; and the studies are too dissimilar to appropriately compare results. Already, Cantor alloy subjected to dynamic strain is known to exhibit improved mechanical behavior [130–132] when compared to Cantor alloy subjected to quasi-static strain. It would be of interest to observe the evolution of the Cantor alloy’s mechanical behavior after phase decomposition and dynamic strain rate mechanical testing. The results of precipitation strengthened CoCrFeMnNi subjected to high strain rates could be promising.

References

[1] Cantor, B., Chang, I. T. H., Knight, P., and Vincent, A. J. B., 2004, "Microstructural Development in Equiatomic Multicomponent Alloys," Mater. Sci. Eng. A, **375–377**, pp. 213–218.

[2] Cantor, B., 2014, "Multicomponent and High Entropy Alloys," Entropy, **16**(9), pp. 4749–4768.

[3] Yeh, J. W., Chen, S. K., Lin, S. J., Gan, J. Y., Chin, T. S., Shun, T. T., Tsau, C. H., and Chang, S. Y., 2004, "Nanostructured High-Entropy Alloys with Multiple Principal Elements: Novel Alloy Design Concepts and Outcomes," Adv. Eng. Mater., **6**(5), pp. 299-303+274.

[4] Ye, Y. F., Wang, Q., Lu, J., Liu, C. T., and Yang, Y., 2016, "High-Entropy Alloy: Challenges and Prospects," Mater. Today, **19**(6), pp. 349–362.

[5] Senkov, O. N., Miller, J. D., Miracle, D. B., and Woodward, C., 2015, "Accelerated Exploration of Multi-Principal Element Alloys with Solid Solution Phases," Nat. Commun., **6**, pp. 1–10.

[6] Callister, W. D., and Rethwisch, D. G., 2006, *Materials Science and Engineering: An Introduction (7th Edition)*, John Wiley & Sons, Ltd, New York.

[7] Tsai, M. H., and Yeh, J. W., 2014, "High-Entropy Alloys: A Critical Review," Mater. Res. Lett., **2**(3), pp. 107–123.

[8] Yeh, J. W., Chen, Y. L., Lin, S. J., and Chen, S. K., 2007, "High-Entropy Alloys – A New Era of Exploitation," Mater. Sci. Forum, **560**, pp. 1–9.

[9] Murty, B. S., Yeh, J. W., and Ranganathan, S., 2014, *High-Entropy Alloys*, Elsevier Science and Technology.

[10] Miracle, D. B., and Senkov, O. N., 2017, “A Critical Review of High Entropy Alloys and Related Concepts,” Acta Mater., **122**, pp. 448–511.

[11] Drake, G. W. F., 2018, “Entropy,” Encycl. Br., pp. 2–4.

[12] Openstax, 2016, “Openstax, Chemistry,” Openstax CNX [Online]. Available: https://opentextbc.ca/chemistry/. [Accessed: 06-Aug-2020].

[13] Lee, C. O., 2020, “Configurational Entropy and Instability of Tachyonic Braneworld,” Phys. Lett. Sect. B Nucl. Elem. Part. High-Energy Phys., **800**, p. 135030.

[14] Gačnik, D., 2017, “High-Entropy Alloys,” University of Ljubljana.

[15] Schaffer, J. P., Saxena, A., Antolovich, S. D., Sanders, T. H. J., and Warner, S. B., 1995, *The Science and Design of Engineering Materials*, Richard D. Irwin.

[16] Yeh, J. W., 2013, “Alloy Design Strategies and Future Trends in High-Entropy Alloys,” JOM, **65**(12), pp. 1759–1771.

[17] Miracle, D. B., Miller, J. D., Senkov, O. N., Woodward, C., Uchic, M. D., and Tiley, J., 2014, “Exploration and Development of High Entropy Alloys for Structural Applications,” Entropy, **16**(1), pp. 494–525.

[18] Yeh, J. W., Chen, S. K., Gan, J. Y., Lin, S. J., Chin, T. S., Shun, T. T., Tsau, C. H., and Chang, S. Y., 2004, “Formation of Simple Crystal Structures in Cu-Co-Ni-Cr-Al-Fe-Ti-V Alloys with Multiprincipal Metallic Elements,” Metall. Mater. Trans. A Phys. Metall. Mater. Sci., **35 A**(8), pp. 2533–2536.

[19] Tong, C. J., Chen, M. R., Chen, S. K., Yeh, J. W., Shun, T. T., Lin, S. J., and Chang, S. Y., 2005, “Mechanical Performance of the AlxCoCrCuFeNi High-Entropy Alloy System with Multiprincipal Elements,” Metall. Mater. Trans. A Phys. Metall. Mater. Sci., **36**(5), pp. 1263–1271.

[20] Senkov, O. N., Wilks, G. B., Miracle, D. B., Chuang, C. P., and Liaw, P. K., 2010, “Refractory High-Entropy Alloys,” Intermetallics, **18**(9), pp. 1758–1765.

[21] Del Grosso, M. F., Bozzolo, G., and Mosca, H. O., 2012, “Determination of the Transition to the High Entropy Regime for Alloys of Refractory Elements,” J. Alloys Compd., **534**, pp. 25–31.

[22] Lucas, M. S., Wilks, G. B., Mauger, L., Muñoz, J. A., Senkov, O. N., Michel, E., Horwath, J., Semiatin, S. L., Stone, M. B., Abernathy, D. L., and Karapetrova, E., 2012, “Absence of Long-Range Chemical Ordering in Equimolar FeCoCrNi,” Appl. Phys. Lett., **100**(25), p. 251907.

[23] Pickering, E. J., and Jones, N. G., 2016, “High-Entropy Alloys: A Critical Assessment of Their Founding Principles and Future Prospects,” Int. Mater. Rev., **61**(3), pp. 183–202.

[24] Praveen, S., Murty, B. S., and Kottada, R. S., 2012, “Alloying Behavior in Multi-Component AlCoCrCuFe and NiCoCrCuFe High Entropy Alloys,” Mater. Sci. Eng. A, **534**, pp. 83–89.

[25] Pradeep, K. G., Wanderka, N., Choi, P., Banhart, J., Murty, B. S., and Raabe, D., 2013, “Atomic-Scale Compositional Characterization of a Nanocrystalline AlCrCuFeNiZn High-Entropy Alloy Using Atom Probe Tomography,” Acta Mater., **61**(12), pp. 4696–4706.

[26] Singh, A. K., and Subramaniam, A., 2014, “On the Formation of Disordered Solid Solutions in Multi-Component Alloys,” J. Alloys Compd., **587**, pp. 113–119.

[27] Jones, N. G., Aveson, J. W., Bhowmik, A., Conduit, B. D., and Stone, H. J., 2014, “On the Entropic Stabilisation of an Al0.5CrFeCoNiCu High Entropy Alloy,” Intermetallics, **54**, pp. 148–153.

[28] Tasan, C. C., Deng, Y., Pradeep, K. G., Yao, M. J., Springer, H., and Raabe, D., 2014, “Composition Dependence of Phase Stability, Deformation Mechanisms, and Mechanical Properties of the CoCrFeMnNi High-Entropy Alloy System,” Jom, **66**(10), pp. 1993–2001.

[29] Schuh, B., Mendez-Martin, F., Völker, B., George, E. P., Clemens, H., Pippan, R., and Hohenwarter, A., 2015, “Mechanical Properties, Microstructure and Thermal Stability of a Nanocrystalline CoCrFeMnNi High-Entropy Alloy after Severe Plastic Deformation,” Acta Mater., **96**, pp. 258–268.

[30] Christofidou, K. A., Pickering, E. J., Orsatti, P., Mignanelli, P. M., Slater, T. J. A., Stone, H. J., and Jones, N. G., 2018, “On the Influence of Mn on the Phase Stability of the CrMnxFeCoNi High Entropy Alloys,” Intermetallics, **92**, pp. 84–92.

[31] Otto, F., Dlouhý, A., Pradeep, K. G., Kuběnová, M., Raabe, D., Eggeler, G., and George, E. P., 2016, "Decomposition of the Single-Phase High-Entropy Alloy CrMnFeCoNi after Prolonged Anneals at Intermediate Temperatures," Acta Mater., **112**, pp. 40–52.

[32] MacDonald, B. E., Fu, Z., Wang, X., Li, Z., Chen, W., Zhou, Y., Raabe, D., Schoenung, J., Hahn, H., and Lavernia, E. J., 2019, "Influence of Phase Decomposition on Mechanical Behavior of an Equiatomic CoCuFeMnNi High Entropy Alloy," Acta Mater.

[33] Otto, F., Yang, Y., Bei, H., and George, E. P., 2013, "Relative Effects of Enthalpy and Entropy on the Phase Stability of Equiatomic High-Entropy Alloys," Acta Mater., **61**(7), pp. 2628–2638.

[34] He, J. Y., Wang, H., Wu, Y., Liu, X. J., Mao, H. H., Nieh, T. G., and Lu, Z. P., 2016, "Precipitation Behavior and Its Effects on Tensile Properties of FeCoNiCr High-Entropy Alloys," Intermetallics, **79**, pp. 41–52.

[35] Liu, W. H., Lu, Z. P., He, J. Y., Luan, J. H., Wang, Z. J., Liu, B., Liu, Y., Chen, M. W., and Liu, C. T., 2016, "Ductile CoCrFeNiMox High Entropy Alloys Strengthened by Hard Intermetallic Phases," Acta Mater., **116**, pp. 332–342.

[36] Liu, W. H., Yang, T., and Liu, C. T., 2018, "Precipitation Hardening in CoCrFeNi-Based High Entropy Alloys," Mater. Chem. Phys., **210**, pp. 2–11.

[37] Miracle, D. B., 2017, "High-Entropy Alloys: A Current Evaluation of Founding Ideas and Core Effects and Exploring 'Nonlinear Alloys,'" JOM, **69**(11), pp. 2130–2136.

[38] Lyu, Z., Lee, C., Wang, S. Y., Fan, X., Yeh, J. W., and Liaw, P. K., 2019, “Effects of Constituent Elements and Fabrication Methods on Mechanical Behavior of High-Entropy Alloys: A Review,” Metall. Mater. Trans. A Phys. Metall. Mater. Sci., **50**(1), pp. 1–28.

[39] Ikeda, Y., Grabowski, B., and Körmann, F., 2019, “Ab Initio Phase Stabilities and Mechanical Properties of Multicomponent Alloys: A Comprehensive Review for High Entropy Alloys and Compositionally Complex Alloys,” Mater. Charact., **147**, pp. 464–511.

[40] Senkov, O. N., Wilks, G. B., Scott, J. M., and Miracle, D. B., 2011, “Mechanical Properties of Nb25Mo25Ta25W25 and V20Nb20Mo20Ta20W20 Refractory High Entropy Alloys,” Intermetallics, **19**(5), pp. 698–706.

[41] Zhou, Y. J., Zhang, Y., Kim, T. N., and Chen, G. L., 2008, “Microstructure Characterizations and Strengthening Mechanism of Multi-Principal Component AlCoCrFeNiTi0.5 Solid Solution Alloy with Excellent Mechanical Properties,” Mater. Lett., **62**(17–18), pp. 2673–2676.

[42] Hsu, C.-Y., Juan, C.-C., Wang, W.-R., Sheu, T.-S., Yeh, J.-W., and Chen, S.-K., 2011, “On the Superior Hot Hardness and Softening Resistance of AlCoCrxFeMo0.5Ni High-Entropy Alloys,” Mater. Sci. Eng. A, **528**(10–11), pp. 3581–3588.

[43] Huo, W., Zhou, H., Fang, F., Hu, X., Xie, Z., and Jiang, J., 2017, “Strain-Rate Effect upon the Tensile Behavior of CoCrFeNi High-Entropy Alloys,” Mater. Sci. Eng. A, **689**, pp. 366–369.

[44] Gludovatz, B., Hohenwarter, A., Catoor, D., Chang, E. H., George, E. P., and Ritchie, R. O., 2014, “A Fracture-Resistant High-Entropy Alloy for Cryogenic Applications,” Science (80-.)., **345**(6201), pp. 1153–1158.

[45] Zaddach, A. J., Scattergood, R. O., and Koch, C. C., 2015, “Tensile Properties of Low-Stacking Fault Energy High-Entropy Alloys,” Mater. Sci. Eng. A, **636**, pp. 373–378.

[46] Chuang, M. H., Tsai, M. H., Wang, W. R., Lin, S. J., and Yeh, J. W., 2011, “Microstructure and Wear Behavior of AlxCo 1.5CrFeNi1.5Tiy High-Entropy Alloys,” Acta Mater., **59**(16), pp. 6308–6317.

[47] Zhang, Y., Zuo, T. T., Tang, Z., Gao, M. C., Dahmen, K. A., Liaw, P. K., and Lu, Z. P., 2014, “Microstructures and Properties of High-Entropy Alloys,” Prog. Mater. Sci., **61**, pp. 1–93.

[48] Chen, S. T., Tang, W. Y., Kuo, Y. F., Chen, S. Y., Tsau, C. H., Shun, T. T., and Yeh, J. W., 2010, “Microstructure and Properties of Age-Hardenable AlxCrFe1.5MnNi0.5 Alloys,” Mater. Sci. Eng. A, **527**(21–22), pp. 5818–5825.

[49] Qiu, X. W., Zhang, Y. P., He, L., and Liu, C. G., 2013, “Microstructure and Corrosion Resistance of AlCrFeCuCo High Entropy Alloy,” J. Alloys Compd., **549**, pp. 195–199.

[50] Qiu, X. W., and Liu, C. G., 2013, “Microstructure and Properties of Al2CrFeCoCuTiNix High-Entropy Alloys Prepared by Laser Cladding,” J. Alloys Compd., **553**, pp. 216–220.

[51] Hemphill, M. A., Yuan, T., Wang, G. Y., Yeh, J. W., Tsai, C. W., Chuang, A., and Liaw, P. K., 2012, "Fatigue Behavior of Al0.5CoCrCuFeNi High Entropy Alloys," Acta Mater.

[52] Holcomb, G. R., Tylczak, J., and Carney, C., 2015, "Oxidation of CoCrFeMnNi High Entropy Alloys," JOM, **67**(10), pp. 2326–2339.

[53] Kumar, N., Ying, Q., Nie, X., Mishra, R. S., Tang, Z., Liaw, P. K., Brennan, R. E., Doherty, K. J., and Cho, K. C., 2015, "High Strain-Rate Compressive Deformation Behavior of the Al0.1CrFeCoNi High Entropy Alloy," Mater. Des., **86**, pp. 598–602.

[54] Diao, H. Y., Feng, R., Dahmen, K. A., and Liaw, P. K., 2017, "Fundamental Deformation Behavior in High-Entropy Alloys: An Overview," Curr. Opin. Solid State Mater. Sci., **21**(5), pp. 252–266.

[55] Licavoli, J. J., Gao, M. C., Sears, J. S., Jablonski, P. D., and Hawk, J. A., 2015, "Microstructure and Mechanical Behavior of High-Entropy Alloys," J. Mater. Eng. Perform., **24**(10), pp. 3685–3698.

[56] Otto, F., Dlouhý, A., Somsen, C., Bei, H., Eggeler, G., and George, E. P., 2013, "The Influences of Temperature and Microstructure on the Tensile Properties of a CoCrFeMnNi High-Entropy Alloy," Acta Mater., **61**(15), pp. 5743–5755.

[57] Gali, A., and George, E. P., 2013, "Tensile Properties of High- and Medium-Entropy Alloys," Intermetallics, **39**, pp. 74–78.

[58] Eißmann, N., Klöden, B., Weißgärber, T., and Kieback, B., 2016, "High-Entropy Alloy CoCrFeMnNi Produced by Powder Metallurgy," World PM 2016 Congr. Exhib., **60**(3), pp. 184–197.

[59] Ritchie, R. O., 2011, "The Conflicts between Strength and Toughness," Nat. Mater., **10**(11), pp. 817–822.

[60] He, J. Y., Zhu, C., Zhou, D. Q., Liu, W. H., Nieh, T. G., and Lu, Z. P., 2014, "Steady State Flow of the FeCoNiCrMn High Entropy Alloy at Elevated Temperatures," Intermetallics, **55**, pp. 9–14.

[61] Laplanche, G., Berglund, S., Reinhart, C., Kostka, A., Fox, F., and George, E. P., 2018, "Phase Stability and Kinetics of σ-Phase Precipitation in CrMnFeCoNi High-Entropy Alloys," Acta Mater., **161**, pp. 338–351.

[62] Stepanov, N., Tikhonovsky, M., Yurchenko, N., Zyabkin, D., Klimova, M., Zherebtsov, S., Efimov, A., and Salishchev, G., 2015, "Effect of Cryo-Deformation on Structure and Properties of CoCrFeNiMn High-Entropy Alloy," Intermetallics, **59**, pp. 8–17.

[63] George, E. P., Curtin, W. A., and Tasan, C. C., 2020, "High Entropy Alloys: A Focused Review of Mechanical Properties and Deformation Mechanisms," Acta Mater., **188**, pp. 435–474.

[64] Tian, M., Wu, C., Liu, Y., Peng, H., Wang, J., and Su, X., 2019, "Phase Stability and Microhardness of CoCrFeMnxNi2-x High Entropy Alloys," J. Alloys Compd., **811**, p. 152025.

[65] Pickering, E. J., Muñoz-Moreno, R., Stone, H. J., and Jones, N. G., 2016, "Precipitation in the Equiatomic High-Entropy Alloy CrMnFeCoNi," Scr. Mater., **113**, pp. 106–109.

[66] Gludovatz, B., George, E. P., and Ritchie, R. O., 2015, "Processing, Microstructure and Mechanical Properties of the CrMnFeCoNi High-Entropy Alloy," JOM, **67**(10), pp. 2262–2270.

[67] Dobeš, F., Hadraba, H., Chlup, Z., Dlouhý, A., Vilémová, M., and Matějíček, J., 2018, "Compressive Creep Behavior of an Oxide-Dispersion-Strengthened CoCrFeMnNi High-Entropy Alloy," Mater. Sci. Eng. A, **732**(June), pp. 99–104.

[68] Vaidya, M., Guruvidyathri, K., and Murty, B. S., 2019, "Phase Formation and Thermal Stability of CoCrFeNi and CoCrFeMnNi Equiatomic High Entropy Alloys," J. Alloys Compd., **774**, pp. 856–864.

[69] Jang, M. J., Praveen, S., Sung, H. J., Bae, J. W., Moon, J., and Kim, H. S., 2018, "High-Temperature Tensile Deformation Behavior of Hot Rolled CrMnFeCoNi High-Entropy Alloy," J. Alloys Compd., **730**(October), pp. 242–248.

[70] Tsai, K.-Y. Y., Tsai, M.-H. H., and Yeh, J.-W. W., 2013, "Sluggish Diffusion in Co-Cr-Fe-Mn-Ni High-Entropy Alloys," Acta Mater., **61**(13), pp. 4887–4897.

[71] Liu, W. H., Wu, Y., He, J. Y., Nieh, T. G., and Lu, Z. P., 2013, "Grain Growth and the Hall–Petch Relationship in a High-Entropy FeCrNiCoMn Alloy," Scr. Mater., **68**(7), pp. 526–529.

[72] Laurent-Brocq, M., Akhatova, A., Perrière, L., Chebini, S., Sauvage, X., Leroy, E., and Champion, Y., 2015, “Insights into the Phase Diagram of the CrMnFeCoNi High Entropy Alloy,” Acta Mater., **88**, pp. 355–365.

[73] Stepanov, N. D., Shaysultanov, D. G., Ozerov, M. S., Zherebtsov, S. V., and Salishchev, G. A., 2016, “Second Phase Formation in the CoCrFeNiMn High Entropy Alloy after Recrystallization Annealing,” Mater. Lett., **185**, pp. 1–4.

[74] Klimova, M. V., Shaysultanov, D. G., Zherebtsov, S. V., and Stepanov, N. D., 2019, “Effect of Second Phase Particles on Mechanical Properties and Grain Growth in a CoCrFeMnNi High Entropy Alloy,” Mater. Sci. Eng. A, **748**, pp. 228–235.

[75] Divinski, S. V., Pokoev, A. V., Esakkiraja, N., and Paul, A., 2018, “A Mystery of ‘Sluggish Diffusion’ in High-Entropy Alloys: The Truth or a Myth?,” Diffus. Found., **17**, pp. 69–104.

[76] Vaidya, M., Trubel, S., Murty, B. S., Wilde, G., and Divinski, S. V., 2016, “Ni Tracer Diffusion in CoCrFeNi and CoCrFeMnNi High Entropy Alloys,” J. Alloys Compd., **688**, pp. 994–1001.

[77] MacDonald, B. E., Fu, Z., Zheng, B., Chen, W., Lin, Y., Chen, F., Zhang, L., Ivanisenko, J., Zhou, Y., Hahn, H., and Lavernia, E. J., 2017, “Recent Progress in High Entropy Alloy Research,” JOM, **69**(10), pp. 2024–2031.

[78] Maier-Kiener, V., Schuh, B., George, E. P., Clemens, H., and Hohenwarter, A., 2017, “Nanoindentation Testing as a Powerful Screening Tool for Assessing Phase Stability of Nanocrystalline High-Entropy Alloys,” Mater. Des., **115**, pp. 479–485.

[79] Chi, C., Yu, H., and Xie, X., 2011, “Advanced Austenitic Heat-Resistant Steels for Ulta-Super-Critical (USC) Fossil Power Plants,” *Alloy Steel – Properties and Use*, E.V. Morales, ed., InTech, pp. 171–201.

[80] Kuboň, Z., Stejskalová, Š., and Kander, L., 2017, “Effect of Sigma Phase on Fracture Behavior of Steels and Weld Joints of Components in Power Industry Working at Supercritical Conditions,” *Austenitic Stainless Steels - New Aspects*, InTech.

[81] Pohl, M., Storz, O., and Glogowski, T., 2007, “Effect of Intermetallic Precipitations on the Properties of Duplex Stainless Steel,” Mater. Charact., **58**(1), pp. 65–71.

[82] Luo, H., Li, Z., Mingers, A. M., and Raabe, D., 2018, “Corrosion Behavior of an Equiatomic CoCrFeMnNi High-Entropy Alloy Compared with 304 Stainless Steel in Sulfuric Acid Solution,” Corros. Sci., **134**, pp. 131–139.

[83] Adomako, N. K., Kim, J. H., and Hyun, Y. T., 2018, “High-Temperature Oxidation Behaviour of Low-Entropy Alloy to Medium- and High-Entropy Alloys,” J. Therm. Anal. Calorim., **133**(1), pp. 13–26.

[84] Shabani, M., Indeck, J., Hazeli, K., Jablonski, P. D., and Pataky, G. J., 2019, “Effect of Strain Rate on the Tensile Behavior of CoCrFeNi and CoCrFeMnNi High-Entropy Alloys,” J. Mater. Eng. Perform., **28**(7), pp. 4348–4356.

[85] Joshi, P., 2019, “Which High-Performance Materials Are Used in Nuclear Reactors?,” Matmatch [Online]. Available: https://matmatch.com/blog/materials-in-nuclear-reactors/. [Accessed: 19-Oct-2020].

[86] Pourgol-Mohamad, M., Mosleh, A., and Modarres, M., 2011, “Structured Treatment of Model Uncertainty in Complex Thermal-Hydraulics Codes: Technical Challenges, Prospective and Characterization,” Nucl. Eng. Des., **241**(1), pp. 285–295.

[87] Shabani, M., 2018, “Effect of Strain Rate on the Tensile Behavior of CoCrFeNi and CoCrFeMnNi High Entropy Alloys,” Clemson University.

[88] Jablonski, P. D., Licavoli, J. J., Gao, M. C., and Hawk, J. A., 2015, “Manufacturing of High Entropy Alloys,” JOM, **67**(10), pp. 2278–2287.

[89] Hemmerich, K. J., 1998, “General Aging Theory and Simplified Protocol for Accelerated Aging of Medical Devices,” Med. Device Diagnostic Ind. Qmed, pp. 1–10.

[90] Saal, J. E., Berglund, I. S., Sebastian, J. T., Liaw, P. K., and Olson, G. B., 2018, “Equilibrium High Entropy Alloy Phase Stability from Experiments and Thermodynamic Modeling,” Scr. Mater., **146**, pp. 5–8.

[91] Nowell, M., 2016, “Finding Grain and Antigrains,” EDAX - AMETEK Mater. Anal. Div., p. 72 [Online]. Available: https://rsc.aux.eng.ufl.edu/_files/documents/965.pdf.

[92] Choi, N., Kulitckii, V., Kottke, J., Tas, B., Choe, J., Yu, J. H., Yang, S., Park, J. H., Lee, J. S., Wilde, G., and Divinski, S. V., 2020, “Analyzing the ‘Non-Equilibrium State’ of Grain Boundaries in Additively Manufactured High-Entropy CoCrFeMnNi Alloy Using Tracer Diffusion Measurements,” J. Alloys Compd., **844**, p. 155757.

[93] Stepanov, N. D., Shaysultanov, D. G., Salishchev, G. A., Tikhonovsky, M. A., Oleynik, E. E., Tortika, A. S., and Senkov, O. N., 2015, “Effect of v Content on Microstructure and Mechanical Properties of the CoCrFeMnNiVx High Entropy Alloys,” J. Alloys Compd., **628**, pp. 170–185.

[94] He, J. Y., Liu, W. H., Wang, H., Wu, Y., Liu, X. J., Nieh, T. G., and Lu, Z. P., 2014, “Effects of Al Addition on Structural Evolution and Tensile Properties of the FeCoNiCrMn High-Entropy Alloy System,” Acta Mater., **62**, pp. 105–113.

[95] MatWeb, “Technical Data Sheets (Stainless Steel),” ASM Aerosp. Specif. Met. Inc. [Online]. Available: http://asm.matweb.com/search/SpecificMaterial.asp?bassnum=MQ316J. [Accessed: 24-Nov-2020].

[96] Sutton, M. A., Orteu, J. J., and Schreier, H. W., 2009, *Image Correlation for Shape, Motion and Deformation Measurements*, Springer.

[97] Tabor, D., 1951, *The Hardness of Metals*, Claredon Press, Madison.

[98] Ashby, M. F., and Jones, D. R. H., 2005, *Engineering Materials 1: An Introduction to Properties, Applications, and Designs*, Butterworth-Heinemann.

[99] Zhang, P., Li, S. X., and Zhang, Z. F., 2011, “General Relationship between Strength and Hardness,” Mater. Sci. Eng. A, **529**(1), pp. 62–73.

[100] Steinmetz, D. R., Jäpel, T., Wietbrock, B., Eisenlohr, P., Gutierrez-Urrutia, I., Saeed-Akbari, A., Hickel, T., Roters, F., and Raabe, D., 2013, “Revealing the Strain-Hardening Behavior of Twinning-Induced Plasticity Steels: Theory, Simulations, Experiments,” Acta Mater., **61**(2), pp. 494–510.

[101] Takakuwa, O., Kawaragi, Y., and Soyama, H., 2013, "Estimation of the Yield Stress of Stainless Steel from the Vickers Hardness Taking Account of the Residual Stress," J. Surf. Eng. Mater. Adv. Technol., **03**(04), pp. 262–268.

[102] Scotti, L., and Mottura, A., 2016, "Interstitial Diffusion of O, N, and C in α-Ti from First-Principles: Analytical Model and Kinetic Monte Carlo Simulations," J. Chem. Phys., **144**(8), pp. 0–9.

[103] Martinavičius, A., Abrasonis, G., Scheinost, A. C., Danoix, R., Danoix, F., Stinville, J. C., Talut, G., Templier, C., Liedke, O., Gemming, S., and Möller, W., 2012, "Nitrogen Interstitial Diffusion Induced Decomposition in AISI 304L Austenitic Stainless Steel," Acta Mater., **60**(10), pp. 4065–4076.

[104] 2015, "Manganese Sulphide Inclusions in Steel: Part One," Total Mater. [Online]. Available: https://www.totalmateria.com/page.aspx?ID=CheckArticle&site=kts&NM=443. [Accessed: 21-Oct-2020].

[105] 2013, "Chromium (Cr) - Properties, Applications," AZoM [Online]. Available: https://www.azom.com/article.aspx?ArticleID=9081. [Accessed: 01-Nov-2020].

[106] Kit, P., and Lam, J., 2016, "Three-Dimensional Investigations of Different Sulfides in Steels by Using Electrolytic Extraction."

[107] Gerold, V., and Karnthaler, H. P., 1989, "On the Origin of Planar Slip in f.c.c. Alloys," Acta Metall., **37**(8), pp. 2177–2183.

[108] Neuhäuser, H., 1975, “Electron Microscopic Studies in the Yield Region of 70/30-α-Brass Single Crystals-II. Estimation of the Dislocation Friction Stress,” Acta Metall., **23**(4), pp. 455–462.

[109] Hong, S. I., and Laird, C., 1990, “Mechanisms of Slip Mode Modification in F.C.C. Solid Solutions,” Acta Metall. Mater., **38**(8), pp. 1581–1594.

[110] Morris, J. W., 2001, “Austenite at Room and Low Temperature, Deformation and Fracture Of,” *Encyclopedia of Materials: Science and Technology*, Elsevier, pp. 398–401.

[111] Laplanche, G., Bonneville, J., Varvenne, C., Curtin, W. A., and George, E. P., 2018, “Thermal Activation Parameters of Plastic Flow Reveal Deformation Mechanisms in the CrMnFeCoNi High-Entropy Alloy,” Acta Mater., **143**, pp. 257–264.

[112] Li, Z., Zhao, S., Ritchie, R. O., and Meyers, M. A., 2019, “Mechanical Properties of High-Entropy Alloys with Emphasis on Face-Centered Cubic Alloys,” Prog. Mater. Sci., **102**, pp. 296–345.

[113] Shen, Y. F., Li, X. X., Sun, X., Wang, Y. D., and Zuo, L., 2012, “Twinning and Martensite in a 304 Austenitic Stainless Steel,” Mater. Sci. Eng. A, **552**, pp. 514–522.

[114] Song, G. S., Ji, K. S., Song, H. W., and Zhang, S. H., 2020, “Microstructure Transformation and Twinning Mechanism of 304 Stainless Steel Tube during Hydraulic Bulging,” Mater. Res. Express, **6**(12), p. 1265h9.

[115] Xu, D. M., Li, G. Q., Wan, X. L., Misra, R. D. K., Yu, J. X., and Xu, G., 2020, "On the Deformation Mechanism of Austenitic Stainless Steel at Elevated Temperatures: A Critical Analysis of Fine-Grained versus Coarse-Grained Structure," Mater. Sci. Eng. A, **773**, p. 138722.

[116] Curtze, S., and Kuokkala, V. T., 2010, "Dependence of Tensile Deformation Behavior of TWIP Steels on Stacking Fault Energy, Temperature and Strain Rate," Acta Mater., **58**(15), pp. 5129–5141.

[117] Joo, S. H., Kato, H., Jang, M. J., Moon, J., Tsai, C. W., Yeh, J. W., and Kim, H. S., 2017, "Tensile Deformation Behavior and Deformation Twinning of an Equimolar CoCrFeMnNi High-Entropy Alloy," Mater. Sci. Eng. A, **689**, pp. 122–133.

[118] Ashby, M. F., 2011, *Materials Selection in Mechanical Design*, Elsevier.

[119] Wu, D., Zhang, J., Huang, J. C., Bei, H., and Nieh, T. G., 2013, "Grain-Boundary Strengthening in Nanocrystalline Chromium and the Hall – Petch Coefficient of Body-Centered Cubic Metals," **68**, pp. 118–121.

[120] Maciejewski, J., 2015, "The Effects of Sulfide Inclusions on Mechanical Properties and Failures of Steel Components," J. Fail. Anal. Prev., **15**(2), pp. 169–178.

[121] Hasan, M. N., Gu, J., Jiang, S., Wang, H. J., Cabral, M., Ni, S., An, X. H., Song, M., Shen, L. M., and Liao, X. Z., 2020, "Effects of Elemental Segregation on Microstructural Evolution and Local Mechanical Properties in a Dynamically Deformed CrMnFeCoNi High Entropy Alloy," Scr. Mater., **190**, pp. 80–85.

[122] Drake, G. W. F., 2020, "Thermodynamics," Encycl. Br., p. 23.

[123] Hsieh, C.-C., and Wu, W., 2012, “Overview of Intermetallic Sigma (σ) Phase Precipitation in Stainless Steels,” ISRN Metall., **2012**, pp. 1–16.

[124] Humphreys, F. J., and Hatherly, M., 2004, *Recrystallization and Related Annealing Phenomena*, Elsevier.

[125] Yvell, K., 2018, *Experimental Studies of Deformation Structures in Stainless Steels Using EBSD*.

[126] Lewis, M. H., 1966, “Precipitation of (Fe, Cr) Sigma Phase from Austenite,” Acta Metall., **14**(11), pp. 1421–1428.

[127] Chen, W. Y., Kirk, M. A., Hashimoto, N., Yeh, J. W., Liu, X., and Chen, Y., 2020, “Irradiation Effects on Al0.3CoCrFeNi and CoCrMnFeNi High-Entropy Alloys, and 316H Stainless Steel at 500 °C,” J. Nucl. Mater., **539**, p. 152324.

[128] Misra, R. D. K., Challa, V. S. A., Venkatsurya, P. K. C., Shen, Y. F., Somani, M. C., and Karjalainen, L. P., 2015, “Interplay between Grain Structure, Deformation Mechanisms and Austenite Stability in Phase-Reversion-Induced Nanograined/Ultrafine-Grained Austenitic Ferrous Alloy,” Acta Mater., **84**, pp. 339–348.

[129] Hättestrand, M., Larsson, P., Chai, G., Nilsson, J. O., and Odqvist, J., 2009, “Study of Decomposition of Ferrite in a Duplex Stainless Steel Cold Worked and Aged at 450-500 °C,” Mater. Sci. Eng. A, **499**(1–2), pp. 489–492.

[130] Li, Z., Zhao, S., Diao, H., Liaw, P. K., and Meyers, M. A., 2017, “High-Velocity Deformation of Al0.3 CoCrFeNi High-Entropy Alloy: Remarkable Resistance to Shear Failure,” Sci. Rep., **7**(February), pp. 1–8.

[131] Meyers, M. A., Li, Z., Zhao, S., Wang, B., Liu, Y., and Liaw, P. K., 2018, "Shear Localization of Fcc High-Entropy Alloys," EPJ Web Conf., **183**, pp. 1–4.

[132] Li, Z., Zhao, S., Alotaibi, S. M., Liu, Y., Wang, B., and Meyers, M. A., 2018, "Adiabatic Shear Localization in the CrMnFeCoNi High-Entropy Alloy," Acta Mater., **151**, pp. 424–431.